Manganese tetraphenylporphyrin bromide and iodide. Studies of structures and magnetic properties

Alexandria N. Bone,[a] Shelby E. Stavretis,[a] J. Krzystek,[b] Zhiming Liu,[a] Qiang Chen,[c] Zheng Gai,[d] Xiaoping Wang,[e] Carlos A. Steren,[a] Xian B. Powers,[a] Andrey A. Podlesnyak,[e] Xue-Tai Chen,[f] Joshua Telser,[g] Haidong Zhou,[c] and Zi-Ling Xue[a,]*

[a] *Department of Chemistry, University of Tennessee, Knoxville, Tennessee 37996, United States*

[b] *National High Magnetic Field Laboratory, Florida State University, Tallahassee, Florida 32310, United States*

[c] *Department of Physics, University of Tennessee, Knoxville, Tennessee 37996, United States*

[d] *Center for Nanophase Materials Sciences and* [e] *Neutron Scattering Division, Oak Ridge National Laboratory, Oak Ridge, Tennessee 37831, United States*

[f] *State Key Laboratory of Coordination Chemistry, School of Chemistry and Chemical Engineering, Nanjing University, Nanjing 210023, China*

[g] *Department of Biological, Physical, and Health Sciences, Roosevelt University, Chicago, Illinois 60605, United States*

Abstract

Manganese tetraphenylporphyrin bromide and iodide Mn(TPP)X (X = Br, **2**; I, **3**; TPP^{2-} = *meso*-tetraphenylporphyrinate) are synthetic analogs of Mn(III) geoporphyrins. Crystal structures of **2** and **3** with chloroform in the lattices, $Mn(TPP)Br\cdot CHCl_3$ (**$2\cdot CHCl_3$**), $Mn(TPP)I\cdot CHCl_3$ (**$3\cdot CHCl_3$**), $Mn(TPP)I\cdot CDCl_3$ (**$3\cdot CDCl_3$**) in a different space group from **$3\cdot CHCl_3$**, $Mn(TPP)I\cdot 1.5CHCl_3$ (**$3\cdot 1.5CHCl_3$**), and **2** with dichloromethane in the lattice, $Mn(TPP)Br\cdot CH_2Cl_2$ (**$2\cdot CH_2Cl_2$**), have been determined by single-crystal X-ray diffraction at 100

K or 298 K. Hirshfeld surface analyses of the crystal structures of **2·CHCl$_3$**, **2·CH$_2$Cl$_2$**, **3·CHCl$_3$**, **3·CDCl$_3$** and **3·1.5CHCl$_3$** have been performed. Surprisingly the Mn(III)–Br and Mn(III)–I bonds in Mn(TPP)X (**2-3**) are about 0.2 Å (8%) longer than Fe(III)–Br and Fe(III)–I bonds in $S = 5/2$ Fe(TPP)X (X = Br, **4**; I, **5**), although both Mn(III) and Fe(III) ions have the same radii. Magnetic properties of **2** and **3** have been studied by direct current (DC) and alternating current (AC) susceptibility measurements, high-field electron paramagnetic resonance (HFEPR), and inelastic neutron scattering (INS). With four unpaired electrons in Mn(TPP)X (X = Br, **2**; I, **3**), the bromide complex **2** in **2·CDCl$_3$** possesses easy-axis anisotropy, as the chloride analog Mn(TPP)Cl (**1**), with the axial (D) and rhombic (E) zero-field splitting parameters of $D = -1.091(3)$ cm^{-1} and $|E| = 0.087(2)$ cm^{-1}. The iodide complex **3** in **3·CDCl$_3$** becomes easy-plane with $D = +1.30(1)$ cm^{-1} and $|E| = 0.010(5)$ cm^{-1}. Axial ZFS parameters D change from $-2.290(5)$ cm^{-1} in **1**, reported earlier, to $-1.091(3)$ cm^{-1} in **2** and $+1.30(1)$ cm^{-1} in **3**.

Keywords: Mn porphyrin complexes; zero-field splitting (ZFS); HFEPR; inelastic neutron scattering (INS); Hirshfeld surface analysis

Highlights:

- Mn porphyrin halides Mn(TPP)X (X = Br, I) crystallize with a variety of solvents
- Mn–X bonds in Mn(TPP)X are surprisingly longer than Fe–X bonds in Fe(TPP)X
- Hirshfeld surface analyses of crystal structures reveal intermolecular interactions
- Axial anisotropy parameters $D < 0$ for Mn(TPP)Br and $D > 0$ for Mn(TPP)I
- Magnitude of the axial anisotropy decreases from Mn(TPP)Cl to Mn(TPP)Br

* Corresponding author: xue@utk.edu

1. Introduction

Manganese porphyrin complexes have been of research interest since the early dates of metalloporphyrin studies [1-15]. Porphyrins containing Mn ions are members of geological porphyrins (geoporphyrins) that occur in nature [16, 17]. Since manganese porphyrin complexes have different spins than their iron analogs, porphyrin complexes of both metals have been studied in part to compare their properties [13, 18]. Mn(III) porphyrins, found in geoporphyrins [17], are typically stable in air [18], while Mn(II) porphyrins such as Mn(TPP) (TPP^{2-} = *meso*-tetraphenylporphyrinate) and its derivatives are readily oxidized by O_2 to Mn(III) porphyrins [7, 9, 10].

Natural porphyrins typically have low symmetry and contain polar substituents, complicating their studies [19]. Tetraphenylporphyrin and other tetraarylporphyrin complexes have been widely used as symmetrically substituted and hydrophobic analogs [20-36]. Five-coordinate tetraphenylporphyrin complexes with single axial ligands, such as Mn(TPP)X (X = Cl, **1**; Br, **2**; I, **3**; Scheme 1) [15, 22], have been synthesized from the exchanges of the acetate ligand in Mn(TPP)(OAc) with halides.

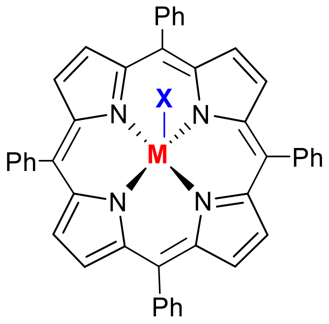

M = Mn; X = Cl, 1; Br, 2; I, 3
M = Fe; X = Br, 4; I, 5

Scheme 1. Structures of M(TPP)X.

For paramagnetic transition metal complexes with spin $S \geq 1$ and quenched angular momenta, one intrinsic magnetic property is the zero-field splitting (ZFS), a second-order spin-orbit coupling (SOC) effect [37]. ZFS is described by the spin-Hamiltonian in Eq. 1 [37, 38].

$$\hat{H} = D\left[\hat{S}_z^2 - S(S+1)/3\right] + E\left(\hat{S}_x^2 - \hat{S}_y^2\right) \qquad \text{(Eq. 1)}$$

where D and E are the axial and rhombic ZFS parameters, respectively.

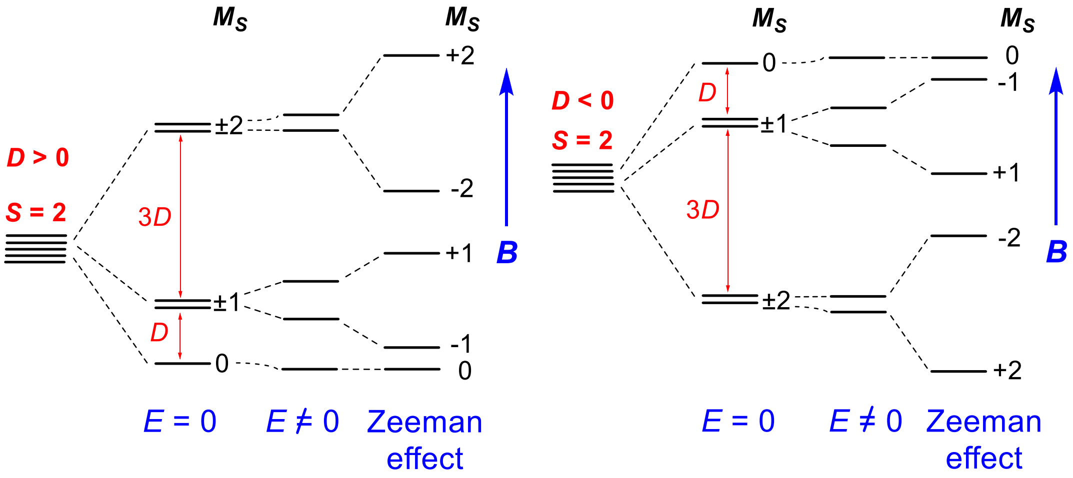

Scheme 2. ZFS in $S = 2$ complexes: $E = 0$ when the crystallographic point group symmetry of the metal site (paramagnetic center) is axial and 3-fold or higher ($x = y \neq z$); $E \neq 0$ when the crystallographic point group symmetry of the metal site is lower than 3-fold ($x \neq y \neq z$) [39]. Inside external magnetic field $\boldsymbol{B}$, Zeeman effect leads to additional splittings [37].

For compounds with both molecular and crystallographic symmetries higher than 2-fold [40], the spin-Hamiltonian in Eq. 1 is simplified into Eq. 2.

$$\hat{H}_s = D\left[\hat{S}_z^2 - S(S+1)/3\right] \qquad \text{(Eq. 2)}$$

For d^4 Mn(III), $S = 2$ complexes, the splitting diagram for five degenerate states is shown in Scheme 2 [37, 38]. When $D > 0$, the spin is mostly located around the *xy* plane (named easy-plane anisotropy), placing the smallest $M_S = 0$ state at ground state. When $D < 0$, the spin is mostly along the *z*-axis (named easy-axis anisotropy), placing the largest $M_S = \pm 2$ states as the ground states. When there is no 4-fold symmetry in either the molecule or the crystal structure, $x \neq y$, the rhombic ZFS parameter $E \neq 0$, leading to splittings shown in Scheme 2. Inside a magnetic field, Zeeman effect leads to the change in the relative energies of the five states (Scheme 2). For an easy-plane ($D > 0$) compound, transitions between the ground $M_S = 0$ and either first excited $M_S = -1$ or second excited $M_S = +1$ state ($\Delta M_S = \pm 1$) are magnetically allowed. For an easy-axis ($D < 0$, $E = 0$) compound inside a magnetic field, the transition from the ground $M_S = -2$ to the first excited $M_S = +2$ state ($\Delta M_S = +4$) is forbidden, as magnetic-allowed transitions have $\Delta M_S = 0$ or ± 1 [41]. Complexes with spin quintet ($S = 2$) ground states and 4-fold molecular and crystallographic symmetries have been historically considered 'EPR-silent' using the criterion of not giving an EPR signal on a spectrometer operating at conventional frequency (generally X-band, e.g., 9.5 GHz). However, when either molecular or crystallographic symmetry is 2-fold or lower, the rhombic ZFS parameter $E \neq 0$, leading to the mixing of the states, as discussed below [37, 38]. In particular, it makes a nominally forbidden transition between the $M_S = |+2\rangle$ and $|-2\rangle$ levels partly allowed, and given the generally small energy difference between these levels, this results in a frequent observation of that transition in X-band at low field [42-45]. Examples of Mn(III) coordination complexes exhibiting such X-band low-field EPR signals are Mn(salen) complexes such as Mn(salen)Cl [42, 43] [salen = (*R,R*)-(−)-N,N'-bis(3,5-di-tert-butylsalicylidene)-1,2-cyclohexanediamine], Mn(acac)$_3$ (acac =

acetylacetonate) [44] and corrole Mn(tpfc) [tpfc = 5,10,15-tris(pentafluorophenyl)corrole trianion] [46]. These signals are usually enhanced by use of parallel mode EPR detection [47, 48], which has also been fruitfully applied to many biological systems containing high-spin Fe(II) ions, also $S = 2$ [48, 49].

Hirshfeld surface analysis has been developed to examine intermolecular interactions in solid, i.e., the interactions of an individual molecule with its nearest neighbor molecules [50-53]. A Hirshfeld surface is an isosurface calculated from the weight function $w(\boldsymbol{r})$ of the sum of spherical atom electron densities in Eq. 3:

$$w(\boldsymbol{r}) = \frac{\rho_{promolecule}(\boldsymbol{r})}{\rho_{procrystal}(\boldsymbol{r})} = \sum_{A \in molecule} \rho_A(\boldsymbol{r}) / \sum_{A \in crystal} \rho_A(\boldsymbol{r}) \qquad \text{(Eq. 3)}$$

where $\rho_{\text{promolecule}}(\boldsymbol{r})$ = sum of the molecular electron density over the atoms in the molecule of interest (the promolecule); $\rho_{\text{procrystal}}(\boldsymbol{r})$ = similar sum over the crystal (the procrystal) [50-53].

The Hirshfeld surface gives a visual 3-*D* representation of the intermolecular close contacts in the crystal. Void volumes in the crystal are readily determined by looking at areas in the crystal where the electron density is the lowest [54]. In comparison, earlier methods are based on the approximation of a molecule as a set of fused spheres with van der Waals radii and are thus limited in scope [50-53]. Hirshfeld surface analysis is an excellent method to study molecular environment and interactions of compounds independent of the overall space group symmetry. We recently used the Hirshfeld surface analysis to study structures of Fe(TPP)Cl and M(TPP)(NO) (M = Fe, Co), revealing that intermolecular interactions are a significant factor in structural disorders of the complexes and phase changes observed in the nitrosyl complexes [34].

Among Mn(TPP)X halide complexes, Mn(TPP)Cl (**1**), a d^4 complex with $S = 2$, has been extensively studied [15, 21-29, 34, 55-64]. In addition to giving solvent-free **1** with 4-fold crystallographic symmetry [40], the porphyrin complex also crystallizes into solvent-containing crystals [57, 65]. Magnetic susceptibility studies of Mn(TPP)Cl·2benzene (**1·2benzene**), Mn(TPP)Cl·benzene (**1·benzene**) and Mn(TPP)Cl·H_2O (**1·H_2O**) showed that it undergoes ZFS with $D = -1.9$ to -2.3 cm^{-1} [23, 63], $-2.2(0.1)$ cm^{-1} [66], and $-2.2(0.1)$ cm^{-1} [66], respectively. Mn(TPP)Cl (**1**) is thus an "EPR silent" (axial) integer spin system, as shown in Scheme 2. Goldberg, Krzystek and coworkers have used high field-EPR (HFEPR) to probe the ZFS of **1**, giving the $D = -2.290(5)$ cm^{-1} [25, 59, 60]. We reported recently an inelastic neutron scattering (INS) study of the transitions among the ZFS states in Mn(TPP)Cl (**1**), confirming (easy-axis) $D = -2.24(3)$ cm^{-1} [28]. Pascual-Álvarez and coworkers have recently shown that Mn(TPP)Cl·benzene (**1·benzene**) undergoes field-induced slow magnetic relaxation [29]. Bromide and iodide analogs Mn(TPP)Br (**2**) and Mn(TPP)I (**3**) have been studied for some time [22], including their structures containing toluene in the lattices, Mn(TPP)Br·toluene (**2·toluene**) and Mn(TPP)I·toluene (**3·toluene**) [11, 12]. However, little is known about their magnetic properties.

We have studied magnetic properties of Mn(TPP)Br (**2**) and Mn(TPP)I (**3**): (a) Mn(TPP)Br·$CHCl_3$ (**2·$CHCl_3$**) and Mn(TPP)I·$CHCl_3$ (**3·$CHCl_3$**) by direct-current (DC) susceptibility measurements; **2·$CHCl_3$** and **3·1.5$CHCl_3$** by alternating-current (AC) susceptibility measurements; (c) **2·$CDCl_3$** and **3·$CDCl_3$** by HFEPR and INS, as part of our investigations of molecular magnetism [28, 35, 67-71]. In the current work, several attempts to grow solvent-free crystals of **2** and **3** instead all gave solvent-containing crystals. We thus crystallized **2** and **3** in deuterated chloroform, yielding **2·$CDCl_3$** and **3·$CDCl_3$**, in order to reduce the number of protons in the unit cells of crystals and thus, background from incoherent neutron scattering by H atoms [72, 73]. In addition, crystallization of **2** in CH_2Cl_2 gave **2·CH_2Cl_2** and **3** in layered pentane/$CHCl_3$ and $CHCl_3$ yielded two different crystals: **3·$CHCl_3$** (in a space group different from that of **3·$CDCl_3$**) and **3·1.5$CHCl_3$**, respectively. Structures of **2·$CHCl_3$**, **2·CH_2Cl_2**, **3·$CHCl_3$**, **3·$CDCl_3$** and **3·1.5$CHCl_3$** have been determined by single-crystal X-ray diffraction. Hirshfeld surface analyses have been conducted for **2·$CHCl_3$**, **2·CH_2Cl_2**, **3·$CHCl_3$**, **3·$CDCl_3$** and **3·1.5$CHCl_3$**.

2. Material and methods

*2.1. Synthesis of Mn(TPP)Br (**2**) and Mn(TPP)I (**3**)*

Mn(TPP)Br (**2**) and Mn(TPP)I (**3**) were prepared by the literature procedure from the exchange reactions between Mn(TPP)(acetate), which was obtained from the reaction of $Mn(CH_3CO_2)_2$ with H_2TPP, and NaX (X = Br, I) in mixed $CHCl_3$-water [15]. $Mn(CH_3CO_2)_2·(H_2O)_4$ (99+%) from Acros Organics, H_2TPP from Frontier Scientific, NaBr (Fisher Scientific, Certified ACS), NaI (Fisher Scientific), N,N-dimethylformamide (Fisher Scientific, Certified ACS) and $CHCl_3$ (Fisher Scientific, Certified ACS) were used as received. Deionized water was obtained in house.

We also prepared Mn(TPP)F by the reported method [15]. However, repeated attempts to purify the product by crystallization failed to yield crystals of Mn(TPP)F. Unlike Mn(TPP)X (X = Cl, **1**; Br, **2**; I, **3**), Mn(TPP)F was found to have low solubility in solvents we tested, including $CHCl_3$ and CH_2Cl_2. Mn(TPP)F may have a polymeric structure, as some other fluoride-bridged complexes [74]. It was not studied further in the current work.

2.2. Crystallization

$CHCl_3$ (Fisher Scientific, Certified ACS), CH_2Cl_2 (Fisher Scientific, Certified ACS), pentane (Fisher Scientific, Certified ACS) and $CDCl_3$ (Cambridge Isotope Laboratories, 99.8% deuterium) were used in the crystallization.

*2.2.1. Mn(TPP)Br·$CHCl_3$ (**2·$CHCl_3$**) and Mn(TPP)Br·$CDCl_3$ (**2·$CDCl_3$**)*

Complex **2** was dissolved in either $CHCl_3$ or $CDCl_3$ and crystals of **2·$CHCl_3$** or **2·$CDCl_3$** grew from concentrated solutions at 23 °C.

*2.2.2. Mn(TPP)Br·CH_2Cl_2 (**2·CH_2Cl_2**)*

Crystals of Mn(TPP)Br·$CHCl_3$ (**2·$CHCl_3$**) were dissolved in a minimal amount of CH_2Cl_2. The solution was left open to air at -33 °C, and crystals of **2·CH_2Cl_2** were harvested from the concentrated solution after several days.

*2.2.3. Mn(TPP)I·$CHCl_3$ (**3·$CHCl_3$**)*

Crystals of Mn(TPP)I·1.5$CHCl_3$ (**3·1.5$CHCl_3$**) were dissolved in a minimal amount of $CHCl_3$ and layered with pentane. Slow mixing of the solvents at room temperature over five days afforded dark green crystals of **3·$CHCl_3$** suitable for single-crystal X-ray analysis.

*2.2.4. Mn(TPP)I·$CDCl_3$ (**3·$CDCl_3$**)*

Newly prepared **3** was dissolved in $CDCl_3$ and crystals of **3·$CDCl_3$** were obtained from the concentrated solution at 23 °C.

*2.2.5. Mn(TPP)I·1.5CHCl₃ (**3·1.5CHCl₃**)*

Impure crystals of **3·1.5CHCl$_3$** were dissolved in CHCl$_3$ and stored at either -33 or 23 °C for recrystallization. Dark green, plate-like crystals of **3·1.5CHCl$_3$** suitable for X-ray analysis were harvested from the concentrated solution.

2.3. Single-crystal X-ray diffraction studies

Single-crystal X-ray diffraction studies of **2·CHCl$_3$**, **2·CH$_2$Cl$_2$**, **3·CHCl$_3$** and **3·1.5CHCl$_3$** were conducted on a Bruker D8 Venture diffractometer equipped with a Photon 100 detector (Mo K_α radiation, $\lambda = 0.71073$ Å). For data collection, a suitable crystal was coated in Paratone oil, mounted on a Mitegen loop, and placed in a cold stream of nitrogen (100 K) generated by an Oxford Cryostream low-temperature apparatus. Frames were collected using the Apex 3 program. The diffraction data were reduced using Bruker SAINT and corrected for absorption with the SADABS multiscan program. The molecular structures were solved with SHELXT and refined with SHELXL-2015.

Single-crystal X-ray diffraction data for Mn(TPP)I·CDCl$_3$ (**3·CDCl$_3$**) were collected on a Bruker ASX Smart 1000 diffractometer with a CCD area detector (Mo K_α radiation, $\lambda = 0.71073$ Å). A suitable crystal was mounted on a goniometer and the data were collected at 293(2) K. Frames were collected using the Apex2 program. Data were reduced using Bruker SAINT and corrected for absorption with the SADABS multiscan program. The molecular structure was solved with SHELXS and refined with SHELXL-2014.

Mn(TPP)Br·CH$_2$Cl$_2$ (**2·CH$_2$Cl$_2$**) crystallizes in the space group $P2_1/n$. There are two Mn(TPP)Br (**2**) molecules and two CH$_2$Cl$_2$ solvent molecules located in general positions of the monoclinic cell. The molecules of **2** form pairs of closely packed of Mn(TPP)Br dimers. One of the two CH_2Cl_2 molecules in the cavities is disordered in two positions with a site-occupancy ratio of 0.751(4) : 0.249(4).

Mn(TPP)I·$CDCl_3$ (**3·$CDCl_3$**) crystallizes in the space group $P2_1/c$. There are two Mn(TPP)I (**3**) and two solvent molecules located in the asymmetric unit of the monoclinic cell. One of the $CDCl_3$ molecules is disordered in three positions with a site-occupancy ratio of 0.328(3) : 0.368(3) : 0.304(3).

Mn(TPP)I·1.5$CHCl_3$ (**3·1.5$CHCl_3$**) crystallizes in the space group *P*-1. There are two Mn(TPP)I molecules located in the asymmetric unit of the triclinic cell. All three chloroform molecules were found disordered in two positions. One displayed about 9.5 degree rotation of the chlorine atoms along the C-H bond with a refined occupancy ratio of 0.814(4) : 0.186(4). Another one showed a displacement less than 1 Å from the main component with 0.325(2) site occupancy. The third chloroform molecule was found disordered around the center of inversion with a site-occupancy ratio of 0.519(1) : 0.481(1).

2.4. Hirshfeld surface calculations

Hirshfeld surfaces were calculated using CrystalExplorer (version 17) software from the crystal-structure coordinates supplied in the format of crystallographic information file (CIF) [75]. The X-ray CIF files of **2·$CHCl_3$** (CCDC 1977356), **2·CH_2Cl_2** (CCDC 1977357), **3·$CHCl_3$** (CCDC 1977355), **3·$CDCl_3$** (CCDC 1977353) and **3·1.5$CHCl_3$** (CCDC 1977354) from the current work and **2·toluene** (CCDC 1168698) [11] and **3·toluene** (CCDC 1168699) [11] in the literature were used. Hirshfeld surfaces were calculated at an isovalue of 0.5 e au^{-3}. Void volumes were calculated using an isovalue of 0.002 e au^{-3} [54]. To perform calculations on disordered structures of $\mathbf{2 \cdot CH_2Cl_2}$, $\mathbf{3 \cdot CDCl_3}$, and $\mathbf{3 \cdot 1.5CHCl_3}$, atomic coordinates with minor partial site occupancies were removed, and the CIF files were regenerated with only atomic coordinates and U^{ij} displacement parameter values.

2.5. Susceptibility measurements

Measurements of DC susceptibilities of $\mathbf{2 \cdot CHCl_3}$, $\mathbf{3 \cdot CHCl_3}$ and Mn(TPP)F were conducted at the University of Tennessee on a Quantum Design MPMS SQUID VSM (Magnetic Property Measurement System Superconducting Quantum Interference Device Vibrating Sample Magnetometer) at the temperature range of 2-300 K within an applied external DC magnetic field of 0.5 T.

Measurements of AC susceptibilities of $\mathbf{2 \cdot CHCl_3}$ and $\mathbf{3 \cdot 1.5CHCl_3}$ were conducted at the Center for Nanophase Materials Sciences (CNMS), Oak Ridge National Laboratory (ORNL) on a Quantum Design Magnetic Property Measurement System XL (MPMS-XL) magnetometer with a 7-T magnet. AC susceptibility measurements were performed at 2.2-7.7 K for $\mathbf{2 \cdot CHCl_3}$ and $\mathbf{3 \cdot 1.5CHCl_3}$ under vacuum with a bias DC field of 0.14 T and 2.74 Oe driving amplitude.

2.6. HFEPR studies of $\mathbf{2 \cdot CDCl_3}$ and $\mathbf{3 \cdot CDCl_3}$

HFEPR measurements were made using a spectrometer described elsewhere [76], with the exception of a solid-state source from Virginia Diodes (Charlottesville, VA). The samples were investigated as pellets mixed with *n*-eicosane. HFEPR spectra were simulated, and computer fits performed, with the program SPIN from A. Ozarowski, using a standard spin Hamiltonian for $S = 2$, with only second-order ZFS terms included.

*2.7. INS studies of **$2\cdot CDCl_3$** and **$3\cdot CDCl_3$***

INS measurements were carried out on Cold Neutron Chopper Spectrometer (CNCS), Spallation Neutron Source (SNS) at ORNL. CNCS is a direct geometry, time-of-flight spectrometer that receives a beam from a coupled cryogenic H_2 moderator [77]. Four chopper assemblies were used to select energy of neutrons at CNCS. The speeds and slit widths of the choppers can be varied, allowing adjustments in the instrumental resolution and intensity of the incident beam.

Approximately 500 mg of each sample of **$2\cdot CDCl_3$** and **$3\cdot CDCl_3$** was loaded into a 1.27-cm-thick aluminum tube which was mounted on a sample holder mounted in a standard liquid helium cryostat with a base temperature of T = 1.7 K. An oscillating radial collimator was used to reduce background scattering form the tail of the cryostat. Vanadium was used as a standard for the detector efficiency correction.

Measurements were performed at 1.7, 10, and 25 K with incident neutron beam energy E_i = 8.07 cm^{-1}. E_i was chosen to cover the anticipated region of interest in both the energy E and scattering-vector Q space [72, 78]. The small incident energy is especially important to observe excitations near the elastic peak (at energy transfer close to 0 cm^{-1}) as the full-width-at-half-maximum (FWHM) of the elastic peak, which is typically 1.5-2% of the incident energy, would be narrow, giving better energy resolution. It took approximately 20 h to run the two samples at various temperatures. Data were then reduced and analyzed using the DAVE (Data Analysis and Visualization Environment) program package [79].

3. Results and discussion

*3.1. Crystal structures of **2·CHCl$_3$**, **2·CH$_2$Cl$_2$**, **3·CHCl$_3$**, **3·CDCl$_3$** and **3·1.5CHCl$_3$***

Crystallographic data of the five structures are given in Table S1 along with their cif files in the supplementary material (SM). Crystal structures of **2·CHCl$_3$** and **3·CHCl$_3$** are discussed below. ORTEP drawings of three other structures, Mn(TPP)X in **2·CH$_2$Cl$_2$**, **3·CDCl$_3$** and **3·1.5CHCl$_3$**, are given in Figs. S1, S2 and S3, respectively with their selected bond lengths and angles in Tables S2, S3 and S4, respectively. Continuous shape measure (CShM) calculations using the SHAPE program [80, 81] were performed on all five structures as well as **2·toluene** and **3·toluene** [11] to analyze the degree of deviation from ideal geometry, and results are provided in Tables S5 and S6.

Crystal of **2·CHCl$_3$** adopts the monoclinic space group $P2_1/n$. ORTEP diagram of the molecule is given in Fig. 1. Selected bond lengths and angles for **2·CHCl$_3$** are included in Table 1. The penta-coordinated Mn^{III} center adopts a distorted square pyramidal geometry with the Mn—Br and four Mn—N bonds in axial and equatorial positions, respectively. In the equatorial plane, the linear N1—Mn1—N3 bonds are slightly elongated [with bond lengths of 2.018(2) and 2.014(2) Å, respectively] than the other N2—Mn1—N4 bonds [bond lengths of 2.001(2) and 2.008(2) Å, respectively]. CShM calculations were performed on the solvent-containing structures of Mn(TPP)Br (**2**) [**2·CHCl$_3$**, **2·toluene** and two independent Mn(TPP)Br (**2**) molecules in **2·CH$_2$Cl$_2$** (Table S5)] show that Mn(TPP)Br molecules in all three analogs exhibit only slight distortion from square pyramidal geometry. Comparison of the Mn—Br bond length here with that of Fe—Br in Fe(TPP)Br (**4**) is given below.

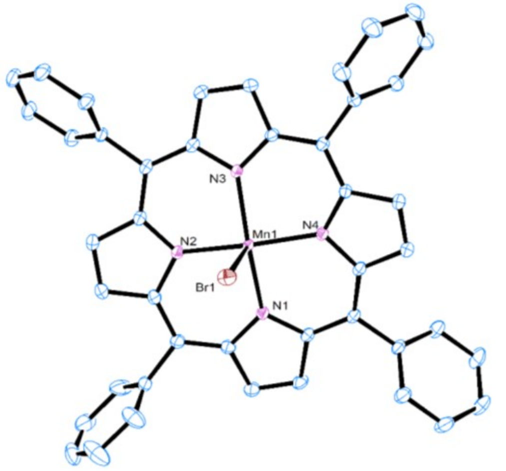

Fig. 1. ORTEP diagram of the structure of Mn(TPP)Br (**2**) in the crystal of **2·CHCl$_3$**. CHCl$_3$ in the lattice and H atoms are omitted.

Table 1. Selected bond lengths (Å) and angles (°) for **2·CHCl$_3$** and **3·CHCl$_3$** at 100(2) K

2·CHCl$_3$		**3·CHCl$_3$**	
Mn1—Br1	2.5363(5)	Mn1—I1	2.7494(4)
Mn1—N1	2.018(2)	Mn1—N1	2.0162(18)
Mn1—N2	2.001(2)	Mn1—N2	2.0148(18)
Mn1—N3	2.014(2)	Mn1—N3	2.0101(18)
Mn1—N4	2.008(2)	Mn1—N4	2.0126(18)
N1—Mn1—Br1	94.60(6)	N1—Mn1—I1	99.36(5)
N2—Mn1—Br1	90.88(7)	N2—Mn1—I1	93.99(5)
N3—Mn1—Br1	100.72(6)	N3—Mn1—I1	96.32(5)
N4—Mn1—Br1	100.77(6)	N4—Mn1—I1	97.16(5)
N1—Mn1—N2	89.98(9)	N1—Mn1—N2	89.42(7)
N2—Mn1—N3	88.73(8)	N2—Mn1—N3	89.27(7)
N3—Mn1—N4	89.37(8)	N3—Mn1—N4	89.06(7)
N4—Mn1—N1	88.81(8)	N4—Mn1—N1	89.21(7)
N1—Mn1—N3	164.64(9)	N1—Mn1—N3	164.32(8)
N2—Mn1—N4	168.35(9)	N2—Mn1—N4	168.83(8)

Mn(TPP)I (**3**) crystallized in layered pentane/$CHCl_3$ solution at 23 °C to give crystals of **3·$CHCl_3$** (monoclinic space group $P2_1/n$). ORTEP diagram of the molecule is given in Fig. 2 with selected bond lengths and angles for **3·$CHCl_3$** in Table 1. The structure shares features with its bromo analog **2·$CHCl_3$** discussed earlier, as comparisons in Table 1 show. CShM calculations of all four structures of Mn(TPP)I (**3**) [**3·$CHCl_3$**, **3·$CDCl_3$**, **3·1.5$CHCl_3$** and **3·toluene**] by the SHAPE program [80, 81] (Table S6) show slight deviations of the Mn(TPP)I molecules (**3**) in all structures from the square pyramid.

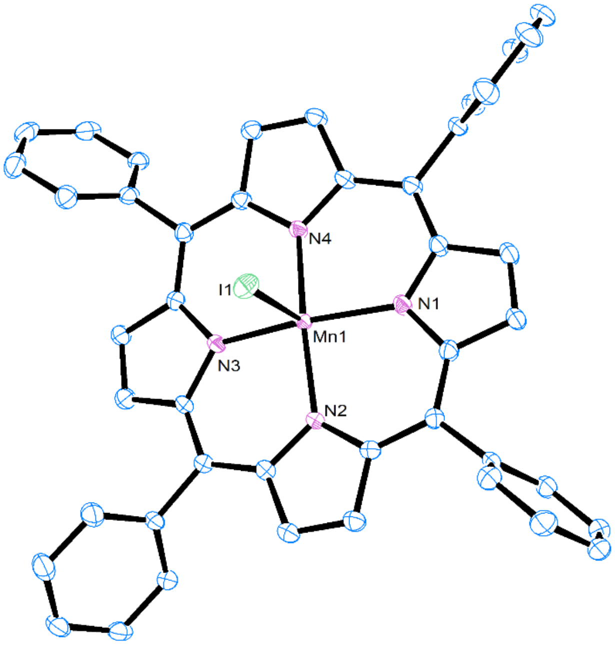

Fig. 2. ORTEP diagram of Mn(TPP)I in **3·$CHCl_3$**. $CHCl_3$ and H atoms are omitted.

Five-coordinate Mn(III) and Fe(III) ions have identical radii of 0.72 Å [82]. Yet, both Mn—Br and Mn—I bonds in Mn(TPP)X (**2-3**) in the crystals (bond lengths of 2.490-2.536 Å and 2.730-2.784 Å, respectively) are about 0.2 Å (or 8%) longer than Fe—Br and Fe—I bonds (bond lengths of 2.348 Å and 2.554 Å, respectively) in Fe(TPP)X (X = **4** [83]; X = I, **5** [84]), as a comparison in Table 2 below shows. This is surprising, as Fe(TPP)X (**4**-**5**) have higher spin (S = 5/2) than Mn(TPP)X (**2**-**3**, S = 2), and the extra d electron in the former resides in an antibonding orbital, as a qualitative MO diagram for the square pyramid complex with C_{4v} symmetry in Scheme S1 shows. The Fe—X bonds in Fe(TPP)X (**4**-**5**) are expected to be longer (not shorter) than the Mn—X bonds in M(TPP)X (**2**-**3**). Extensive studies of octahedral spin crossover complexes [85] and metalloporphyrins [86] have shown that high-spin complexes have more elongated M—L bonds than low-spin complexes as a result of adding electrons to antibonding $d_{x^2-y^2}$ and/or d_{z^2} orbitals, although the comparison here involves complexes of the same metal ions. Another difference between the structures of Mn(TPP)X (**2**-**3**) and its iron(III) analogs Fe(TPP)X (**4**-**5**) is that the former have smaller distances between the Mn(III) ions and the center of the TPP^{2-} ligand [0.236-0.295 Å for Mn(TPP)Br (**2**) and 0.213-0.259 Å for Mn(TPP)I (**3**)] than those [0.489 Å for Fe(TPP)Br (**4**) and 0.459 for Fe(TPP)I (**5**)] in the latter. In fact, the X^{-}–TPP^{2-} (center) distances of 2.760-2.785 Å in Mn(TPP)Br (**2**) and 2.954-3.041 Å in Mn(TPP)I (**3**) are similar to 2.837 Å in Fe(TPP)Br (**4**) and 3.013 Å in Fe(TPP)I (**5**), as shown in Table 2. In other words, the shorter Fe—X bond lengths are compensated by the longer Fe—TPP^{2-} (center) distances. Temperatures, affecting crystal structures, are known to change Hirshfeld surfaces and volumes [34]. However, Hirshfeld surfaces and volumes of Mn(TPP)X (surfaces and volumes are 637.8-656.7 Å^2 and 816.6-845.8 Å^3 for **2**; 648.7-662.3 Å^2 and 826.6-858.0 Å^3 for **3**) with different solvents and temperatures [100(2) or 293-298 K] are similar to those of Fe(TPP)X (**4**-**5**) at 293-295 K with no solvent, as shown in Table 2 and discussed below. The average lengths of the Mn—N bonds in Mn(TPP)X (**2**-**3**) [between the Mn(III) ions and N atoms in the TPP^{2-} ligands] are similar at 2.002-2.010 Å. The Mn—N bonds are slightly shorter than 2.066-2.069 Å of the Fe—N bonds in Fe(TPP)X (**4**-**5**).

Table 2. Comparison of structure features, including Hirshfeld areas, Hirshfeld volumes and void volumes, and spin Hamiltonian parameters[a]

Complexes	**Temp (K) (X-ray diffraction)**	**Space group**	**No. of M(TPP)X molecules per unit cell**	**M ion**	**Hirshfeld area ($\AA^2$)**	**Hirshfeld volume ($\AA^3$)**	**Void volume in the cell volume (%)**	**M-X bond length (Å)[b]**	**Distance from M to the TPP^{2-} plane (Å)[c]**	**Distance from X to the TPP^{2-} plane (Å)[d]**	**ZFS parameters (cm^{-1})**	***g* parameters**
Mn(TPP)Cl (**1**)	293(2)		2	Mn	The reported structure [40] is isomorphous to that of disordered Fe(TPP)Cl [28, 34]. For Hirshfeld analysis of the disorder in the structure of Fe(TPP)Cl, see Ref. [34]						$D = -2.290(5)$ (HFEPR) [60] $D = -2.24(3)$ (INS) [28][e]	$g_\parallel = 1.98(2)$ $g_\perp = 2.005(3)$ [60]
Mn(TPP)Br·CHCl$_3$ (**2·CHCl$_3$**)	100(2)	$P2_1/n$	4	Mn1	643.0	819.6	12.22	2.536	0.236	2.760		
2·CDCl$_3$											$D = -1.091(3)$ $\lvert E\rvert = 0.087(2)$ (HFEPR)	$g_x = 1.996(4)$ $g_y = 1.985(5)$ $g_z = 1.994(2)$
2·CH$_2$Cl$_2$	100(2)	$P2_1/n$	8	Mn1	655.7	821.6	11.66	2.525	0.244	2.762		
				Mn2	637.8	816.6		2.520	0.264	2.775		
2·toluene	298 [11]	$P2_1/m$	2	Mn	656.7	845.8	15.79	2.490	0.295	2.785		
Mn(TPP)I·CHCl$_3$ (**3·CHCl$_3$**)	100(2)	$P2_1/n$	4	Mn1	662.3	849.2	14.12	2.749	0.235	2.983		
3·CDCl$_3$	293(2)	$P2_1/c$	8	Mn1	654.0	850.6	14.63	2.744	0.232	2.969	$D = +1.30(1)$ $\lvert E\rvert = 0.010(5)$ (HFEPR)	$g_x = 1.965(5)$ $g_y = 1.971(10)$ $g_z = 1.930(5)$
				Mn2	648.7	846.0		2.748	0.225	2.972		
3·1.5CHCl$_3$	100(2)	$P\bar{1}$	4	Mn1	656.5	834.8	12.61	2.742	0.213	2.954		
				Mn2	651.4	826.6		2.784	0.259	3.041		
3·toluene	298 [11]	$P\bar{1}$	4	Mn1a	657.8	852.0	14.56	2.767	0.239	3.006		
				Mn1b	659.4	858.0		2.730	0.252	2.979		
Fe(TPP)Br (**4**)	295 [83]	$P2_1/c$	4	Fe1				2.348	0.489	2.837	$D = +8.8(2)$ $\lvert E\rvert = 0.1(2)$ (INS) [35]	
Fe(TPP)I (**5**)	293 [84]	$P2_1/n$	4	Fe1				2.554	0.459	3.013	$D = +13.4(6)$ $\lvert E\rvert = 0.3(6)$ (INS) [35]	

[a] Unless cited, the data are from the current work.

[b] Four significant digits of the bond lengths are used here, and estimated standard deviations (esd) are not listed. For the precise bond lengths, see tables listing bond lengths of the structures or the original publications.

[c] The distances here are from the metal ions to the centers of the least-square planes defined by the four N atoms of the TPP^{2-} ligands.

[d] The distances here are from the halide atoms to the centers of the least-square planes defined by the four N atoms of the TPP^{2-} ligands.

[e] Magnetic susceptibility measurements of Mn(TPP)Cl·benzene (**1·benzene**) [66], Mn(TPP)Cl·2benzene (**1·2benzene**) [23] and Mn(TPP)Cl·H$_2$O (**1·H$_2$O**) [66] gave $D = -2.2(2)$, $-2.3(5)$ and $-2.3(2)$ cm^{-1}, respectively. The g values for **1·benzene** and **1·H$_2$O** are 2.01(1) and 2.00(1), respectively [66].

3.2. Hirshfeld surface analyses

Hirshfeld surface analyses and fingerprint plots of Mn(TPP)Br·$CHCl_3$ (**2·$CHCl_3$**, Figs. 3-4) and Mn(TPP)I·$CHCl_3$ (**3·$CHCl_3$**, Figs. 5-6) are discussed below, with the analyses of **2·CH_2Cl_2** (Figs. S4-S5), **3·$CDCl_3$** (Figs. S9-S10) and **3·1.5$CHCl_3$** (Figs. S11-S12) given in SM. We have conducted Hirshfeld surface analyses of the reported structures of **2·toluene** (Figs. S6-S7) and **3·toluene** (Figs. S13-S14). The results are provided in SM. Views of the Hirshfeld surfaces for these structures (e.g., Figs. 3 and 5) show that they all have sites of close contacts (red spots). In addition to a comparison of structure features, Hirshfeld areas, Hirshfeld volumes and void volumes in Table 2, Figs. S8 and S15 give percentage contributions to the Hirshfeld surface areas for various intermolecular close contacts for Mn(TPP)Br (**2**) and Mn(TPP)I (**3**) molecules, respectively, in various crystal structures.

Hirshfeld analyses of the single molecule in the unit cell of Mn(TPP)Br·$CHCl_3$ (**2·$CHCl_3$**) in the $P2_1/n$ space group (100 K) give areas and volumes 643.0 Å^2 and 819.6 Å^3 (Fig. 3, Table 2), respectively, that are similar to those (637.8-655.7 Å^2 and 816.6-821.6 Å^3, Fig. S4, Table 2) of the two independent molecules in the unit cell of **2·CH_2Cl_2** which is also in the $P2_1/n$ space group (100 K). The two structures also have similar percent void volumes (12.22% and 11.66% for **2·$CHCl_3$** and **2·CH_2Cl_2**, respectively). Hirshfeld fingerprint plots in Figs. 4 and S5 for **2·$CHCl_3$** and **2·CH_2Cl_2**, respectively, emphasize close intermolecular interactions. For both structures with different solvent molecules, the H···H and H···Br close contacts involving **2** in **2·$CHCl_3$** (Fig. 4) and the Mn1 molecule in **2·CH_2Cl_2** (Fig. S5-Top) are fairly similar to each other and to those in **2·toluene** at 298 K (Fig. S7) containing non-halogen solvent toluene. The molecules of Mn1 and Mn2 in **2·CH_2Cl_2** form pairs of Mn1...Mn1 and Mn2...Mn2 dimers in which the Mn-Br bonds point inwards with each other in each of the dimer units. Br1 in the

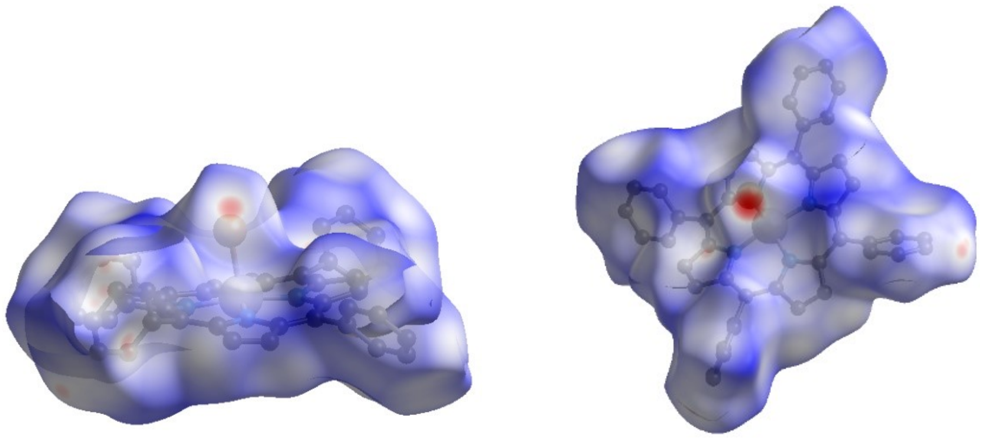

Fig. 3. Two views of the Hirshfeld surface of **2·CHCl₃** showing normalized close distances of the pro-molecule and neighboring molecules at 100(2) K [51]. The red-white-blue coloring scheme demonstrates decreasing contacts. Sites of close contacts are shown in red dots. Semi-transparent view reveals the enclosed molecule. Hereafter the same below for the coloring scheme, sites of close contacts and semi-transparent view.

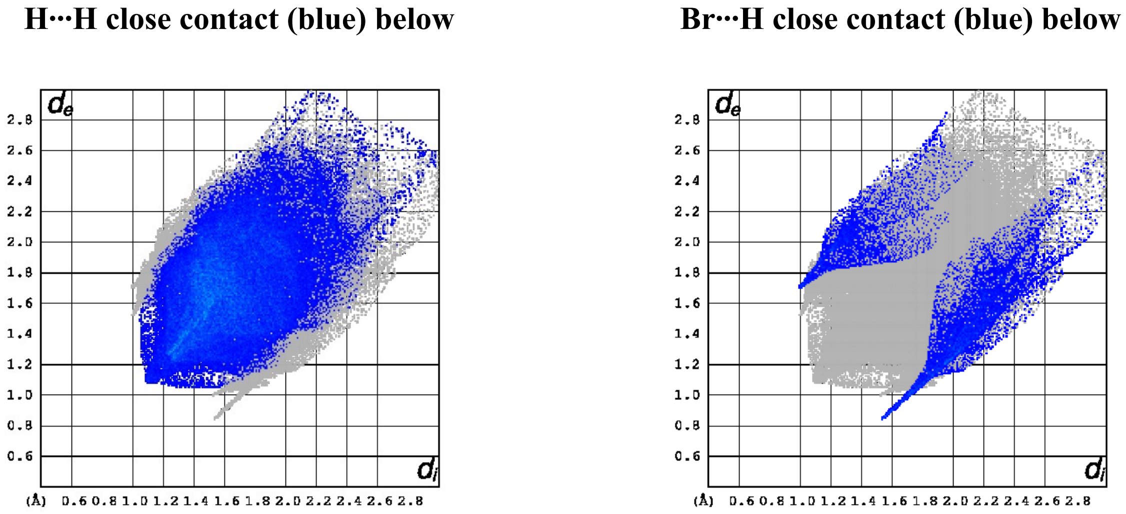

H···H close contact (blue) below

Br···H close contact (blue) below

Fig. 4. Hirshfeld fingerprint plots for **2·CHCl₃**. The closest contacts correspond to the minimum $d_i + d_e$ values in each plot, hereafter the same below. d_i and d_e are distances from the Hirshfeld surface to the nearest atom *interior* and *exterior* to the surface, respectively [52].

molecule of Mn1 has close contact to the terminal H atoms on a phenyl ring of the adjacent Mn1 molecule. In the molecule of Mn2, one of the phenyl groups is facing Br2 with much longer Br2…H(phenyl) distances. The difference in the Hirshfeld fingerprint plots for the Br···H close contacts in Fig. S5 reflects the packing difference of Mn1 and Mn2 molecules in **2·CH_2Cl_2**.

Although both Hirshfeld surfaces and fingerprint plots for the structures of **3·$CHCl_3$** ($P2_1/n$) and **3·1.5$CHCl_3$** ($P\bar{1}$) determined at 100(2) K reveal sites of close contacts (Figs. 5 and S11) and similar H···H and I···H close contacts (Figs. 6 and S12), the Hirshfeld surface area (662.3 $Å^2$) and volume (849.2 $Å^3$) in **3·$CHCl_3$** are slightly larger than those (651.4-656.5 $Å^2$ and 826.6-834.8 $Å^3$) of both independent Mn(TPP)I (**3**) molecules in **3·1.5$CHCl_3$** (Table 2). Structures of both Mn(TPP)I·$CDCl_3$ (**3·$CDCl_3$** in $P2_1/c$) and **3·toluene** ($P\bar{1}$) [11] were determined at room temperatures. Since the D atom in $CDCl_3$ has the same electron density as an H atom, the D atom was refined as an H atom. The two independent molecules in the unit cells of both crystals show sites of close contacts (Figs. S9 and S13). Although the patterns of fingerprint plots for the two are similar, the minimum $d_i + d_e$ I···H/D values of about 2.6-2.7 Å in **3·$CDCl_3$** (Fig. S10), indicating the closest I···H/D contacts, are smaller than about 3.0-3.1 Å in **3·toluene** (Fig. S14).

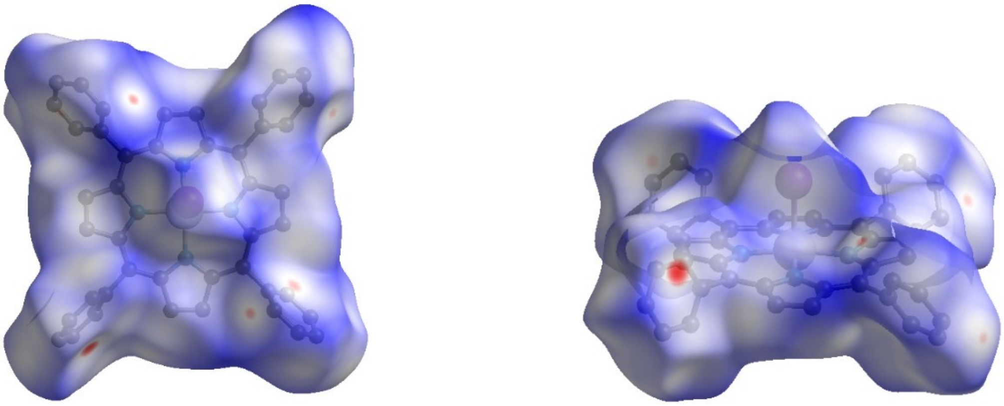

Fig. 5. Two views of the Hirshfeld surface of **3·$CHCl_3$** showing normalized close distances of the pro-molecule and neighboring molecules at 100(2) K [51].

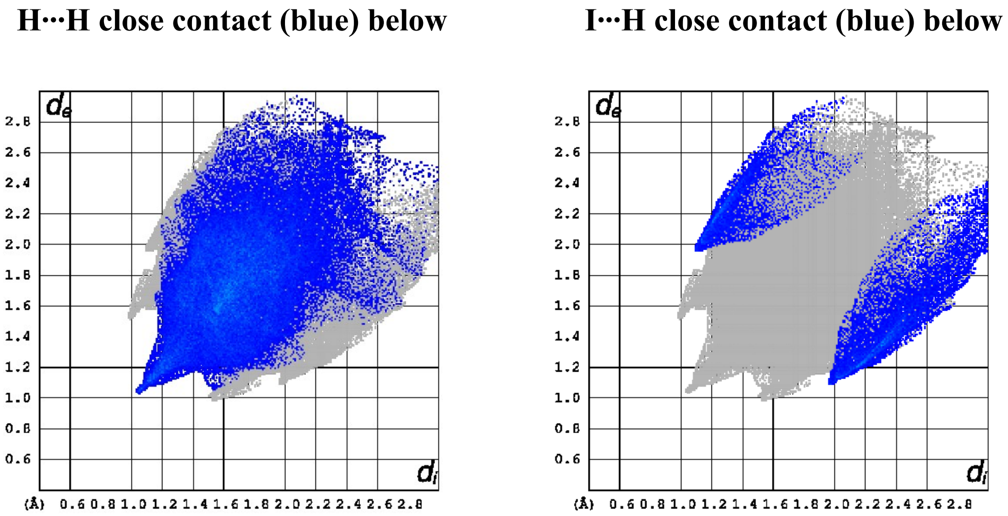
H···H close contact (blue) below

I···H close contact (blue) below

Fig. 6. Hirshfeld fingerprint plots for **3·$CHCl_3$**.

3.3. Magnetic susceptibility

DC magnetic susceptibility χ versus temperature T for Mn(TPP)Br·$CHCl_3$ (**2·$CHCl_3$**) measured between 2 and 300 K in an applied magnetic field of 0.5 T is given as a plot of $\chi_M T$ versus T in Fig. 7-Left, yielding effective magnetic moment $\mu_{eff} \approx 5.2$ BM. Volatile $CHCl_3$ molecules in the lattice are expected to be partially (or completely) removed before and/or in the measurements, as the experiments were conducted under vacuum (~5 torr). If the same data were processed for solvent-free Mn(TPP)Br (**2**) as shown in Fig. S16-Left, they gave effective magnetic moment $\mu_{eff} \approx 4.6$ BM. For a spin-only, $S = 2$ complex, $\mu_{eff} = 4.9$ BM is expected. Thus, $\mu_{eff} \approx 5.2$ and 4.6 BM calculated for **2·$CHCl_3$** and solvent-free **2**, respectively, are about 7% higher and lower than 4.9 BM. The discrepancies here suggest that a significant portion of the solvent $CHCl_3$ molecules in the lattice was removed under vacuum (5 torr) during the measurements. Upon cooling below 20 K, $\chi_M T$ exhibits a sharp decrease from a constant 3.259 $cm^3 \cdot K \cdot mol^{-1}$ to 2.561 $cm^3 \cdot K \cdot mol^{-1}$ at 2 K. This decrease is likely due to ZFS of the Mn(III) ion in the complex, as observed for **1** [29]. An M-H plot of **2·$CHCl_3$** is given in Fig. S17-Top. No frequency-dependent out-of-phase signals (χ_M'') were observed with the AC frequency of 1-1488.1 Hz at 1.8 K using 0 or 0.14 magnetic field (Figure S17-Bottom), suggesting that **2·CHCl$_3$** does not exhibit SMM properties.

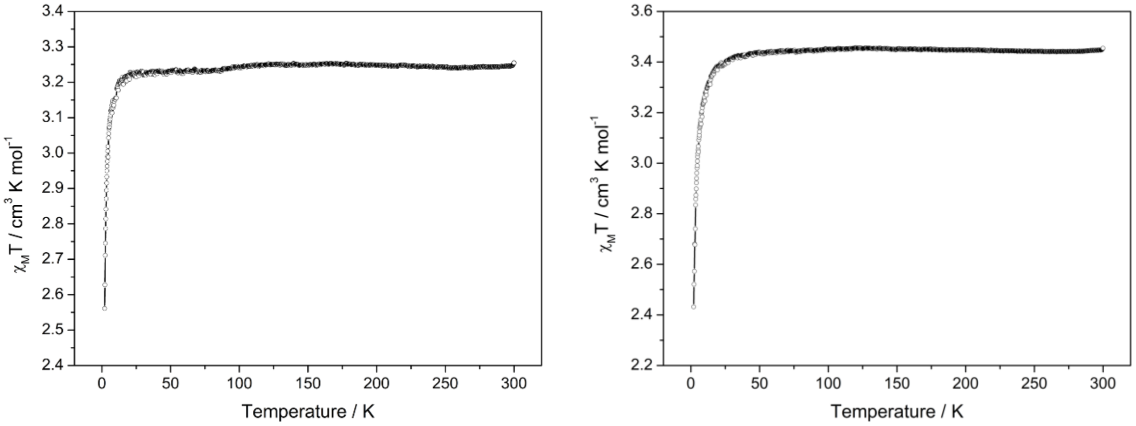

Fig. 7. Variable-temperature DC susceptibility data under applied DC field of 0.5 T: (Left) **2·CHCl$_3$**. (Right) **3·CHCl$_3$**. The lines are guides to the eye.

DC susceptibility data of Mn(TPP)I·CHCl$_3$ (**3·CHCl$_3$**) give plots such as those in Fig. 7-Right for data at 0.5 T, yielding $\mu_{\text{eff}} \approx 5.5$ BM. However, if the same data were processed for solvent-free **Mn(TPP)I** (Fig. S16-Right), $\mu_{\text{eff}} \approx 4.9$ BM. The results suggest that nearly all CHCl$_3$ molecules in **3·CHCl$_3$** were removed before or during the measurements. Like **2·CHCl$_3$**, **3·CHCl$_3$** exhibits a decrease in $\chi_M T$ from 3.454 cm^3·K·mol^{-1} to 2.432 cm^3·K·mol^{-1} upon cooling below 50 K; this may also be attributed to the ZFS of the Mn(III) complex. An M-H plot of **3·1.5CHCl$_3$** is given in Fig. S18-Top. AC susceptibility measurements of **3·1.5CHCl$_3$** show no slow magnetic relaxation (Fig. S18-Bottom).

3.4. HFEPR studies

HFEPR response of Mn(TPP)Br·$CDCl_3$ (**2·$CDCl_3$**) represents powder spectra of an $S = 2$ spin species with moderate negative ZFS on the order of -1 cm^{-1}. Fig. 8-Top shows a typical spectrum recorded at 10 K, and at the highest end of frequencies used, 322 GHz, along with its simulations. Two more spectra, recorded at lower frequencies, are shown in Fig. S19-Top and Fig. S20-Top in the supplementary material (SM). Although the spectra show a presence of more than one species, spin Hamiltonian parameters for the dominant species could be well established using tunable-frequency EPR methodology [87], as shown in Fig. 9-Top. Spin Hamiltonian parameters obtained from computer fits, and used in the simulations, are collected in Table 2. From a visual comparison of the single-frequency spectra and the two cases of simulations for each of them, one for $D < 0$, and the other $D > 0$, it is apparent that D is *negative* in Mn(TPP)Br·$CDCl_3$ (**2·$CDCl_3$**).

HFEPR response of Mn(TPP)I·$CDCl_3$ (**3·$CDCl_3$**) is very different from that of Mn(TPP)Br·$CDCl_3$ (**2·$CDCl_3$**). Fig. 8-Bottom shows a typical spectrum recorded at 10 K, and at the same frequency as the bromide analog, 322 GHz, along with its simulations. Two more spectra, recorded at lower frequencies, are shown in Fig. S19-Bottom and Fig. S20-Bottom in SM. Although the quality of the spectra is somewhat lower than that of **2·$CDCl_3$**, and there is noticeable presence of a minority spin species, it is beyond doubt that the sign of D in Mn(TPP)I·$CDCl_3$ (**3·$CDCl_3$**) is *positive*. In addition, both single-frequency spectra and the 2-D field vs. frequency (energy map) (Fig. 9-Bottom) show that the g-values in **3·$CDCl_3$** (1.93-1.97) are markedly lower than 1.99-2.01 which are the usual numbers found in Mn coordination complexes at any oxidation state.

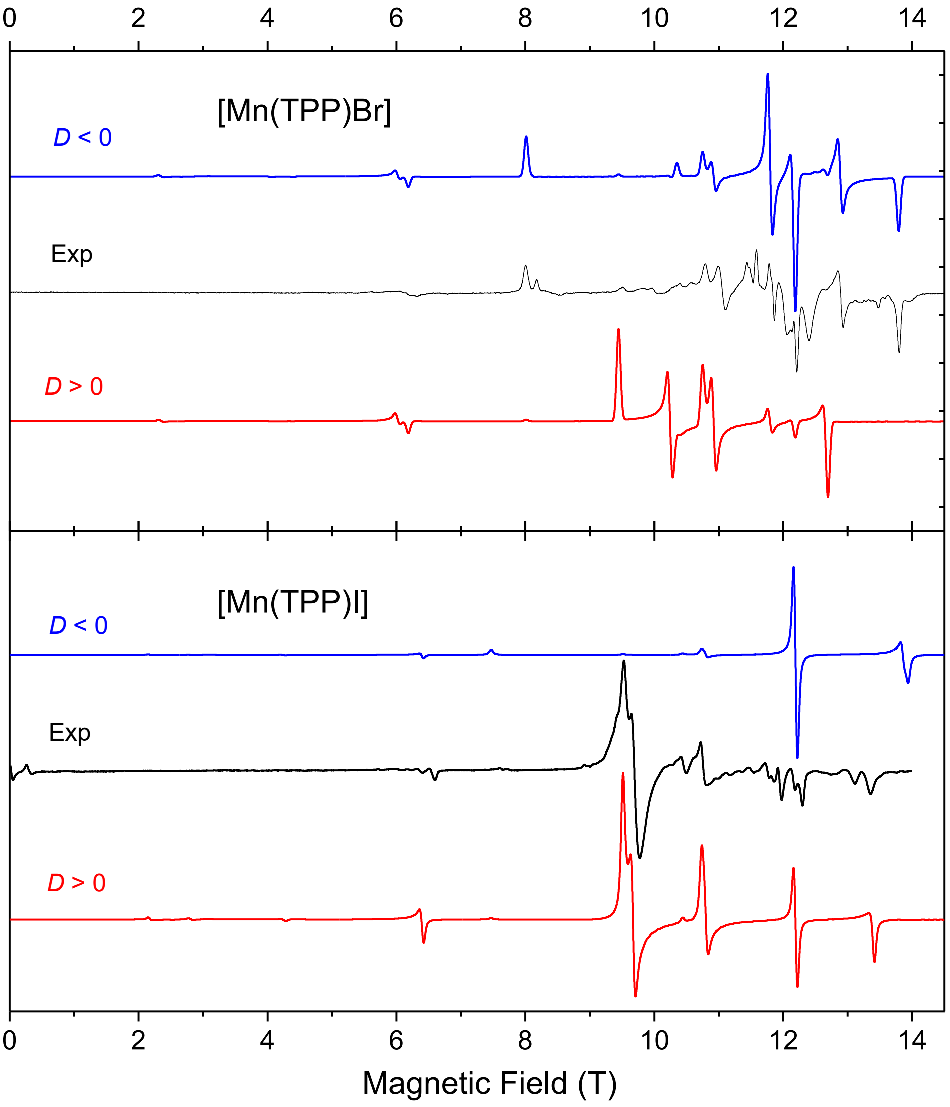

Fig. 8. HFEPR spectra of Mn(TPP)Br·$CDCl_3$ (**2·$CDCl_3$**, Top) and Mn(TPP)I·$CDCl_3$ (**3·$CDCl_3$**, Bottom) at 10 K and 321.6 GHz (black traces) and their powder-pattern simulations (colored traces). The spin Hamiltonian parameters used in simulations were the same as in Table 2 for **2·$CDCl_3$** and slightly adjusted for **3·$CDCl_3$**: $D = +1.34$ cm^{-1}, $E = +0.013$ cm^{-1} ($E/D = 0.01$); $g = [1.965(5), 1.971(10), 1.930(5)]$. Blue traces: $D < 0$; red traces: $D > 0$. Two near-zero field resonances in the spectrum of **3·$CDCl_3$** indicate a minority spin species with ZFS on the order of 4 cm^{-1}, typical for octahedrally-coordinated Mn(III) ions.

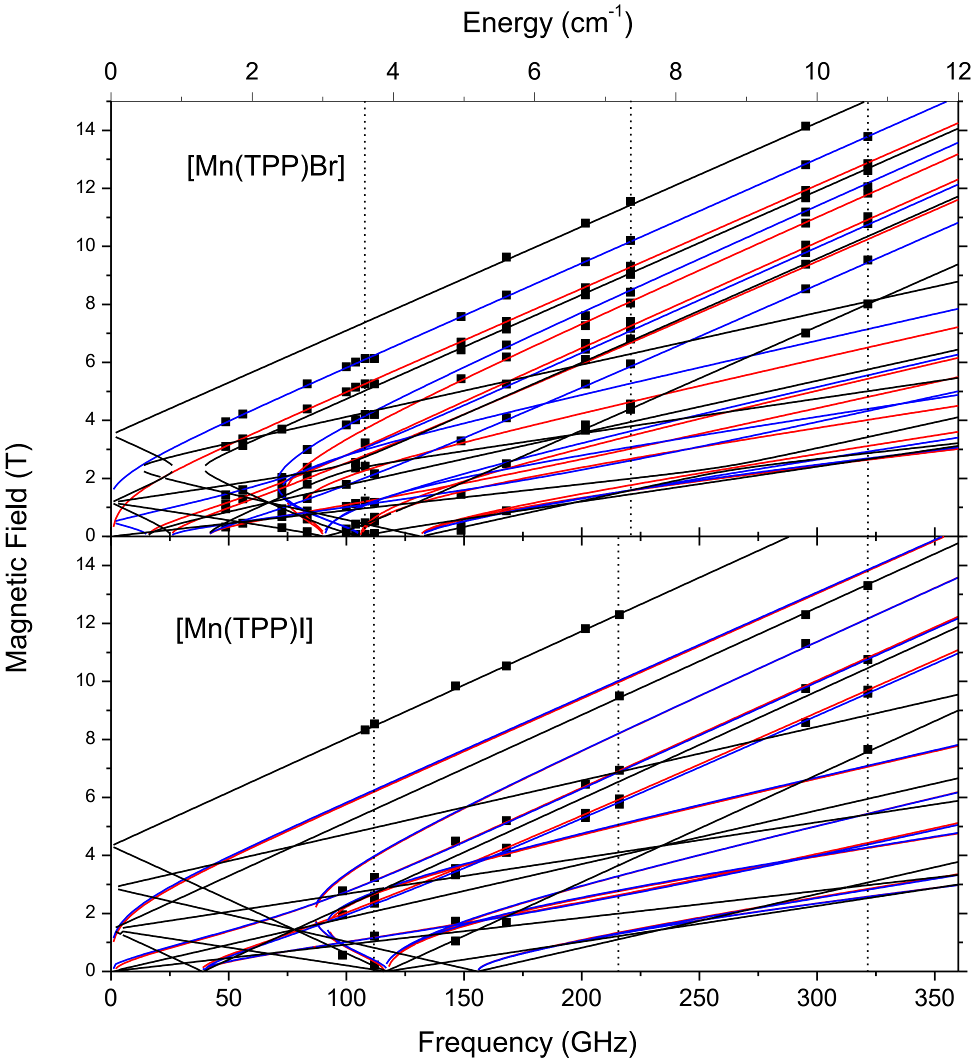

Fig. 9. 2-D field/frequency (energy) maps of turning points in HFEPR spectra of Mn(TPP)Br·$CDCl_3$ (**2·$CDCl_3$**) (Top) and Mn(TPP)I·$CDCl_3$ (**3·$CDCl_3$**) (Bottom, black squares in each case). The curves are simulations using spin Hamiltonian parameters as in Table 2. Red curves: turning points with magnetic field parallel to the *x* axis of the ZFS tensor; blue: $B_0 \parallel y$; black: $B_0 \parallel z$. Off-axis turning points, of which there are several depending on frequency, are not plotted as they were not used in the fits. The vertical dashed lines represent frequencies, at which spectra shown in Fig. 12-Top, Fig. S19-Top (in SM) and Fig. S20-Top for **2·$CDCl_3$** and Fig. 12-Bottom, Fig. S19-Bottom and Fig. S20-Bottom for **3·$CDCl_3$**.

Although molecules of Mn(TPP)Br (**2**) and Mn(TPP)I (**3**) have 4-fold symmetry, crystals of Mn(TPP)Br·$CHCl_3$ (**2·$CHCl_3$**, *P*21/*n*) and Mn(TPP)I·$CDCl_3$ (**3·$CDCl_3$**, *P*21/*c*) do not have 4-fold symmetry. Although the structure of **2·$CDCl_3$** used for the HFEPR studies was not directly determined, it is expected to be in a monoclinic space group. Since in monoclinic unit cells, $x \neq y$, additional ZFS occurs, as shown in Eq. 1. Thus, in addition to axial ZFS parameters D, both **2·$CDCl_3$** and **3·$CDCl_3$** have rhombic ZFS parameters E, as observed in the HFEPR spectra.

3.5. INS studies

In neutron scattering processes, the incident neutrons are scattered from interactions with either atomic nuclei or unpaired electrons in the sample [72, 77, 88]. The cross section of magnetic scattering, from the interactions between neutron spins and electron spins, corresponds to the number of neutrons scattered per second due to the magnetic interaction into a solid angle $d\Omega$ with energy transfer between $\hbar\omega$ and $\hbar(\omega + d\omega)$ divided by the flux of the incident neutrons. If unpolarized neutrons are scattered from identical magnetic ions with localized electrons, the magnetic scattering cross section for spin-only scattering is expressed by Eq. 4 [35, 72, 78].

$$\frac{d^2\sigma}{d\Omega d\omega} = (\gamma r_0)^2 \frac{k_f}{k_i}\left[\frac{1}{2} g F(Q)^2 e^{-2W(Q)} \sum_{\alpha,\beta}\left(\delta_{\alpha\beta} - \frac{Q_\alpha \cdot Q_\beta}{Q^2}\right) S^{\alpha\beta}(Q,\omega)\right] \qquad \text{(Eq. 4)}$$

where σ = neutron cross section; γ = gyromagnetic ratio; r_0 = classical radius of an electron; g = Landé g-factor; $F(\boldsymbol{Q})$ = dimensionless magnetic form factor defined as the Fourier transform of the normalized spin density associated with magnetic ions; $e^{-2W(\boldsymbol{Q})}$ = Debye-Waller factor caused by thermal motion; $S^{\alpha\beta}(\boldsymbol{Q},\omega)$ = magnetic scattering function; $\left(\delta_{\alpha\beta} - \frac{\boldsymbol{Q}_\alpha \boldsymbol{Q}_\beta}{Q^2}\right)$ = polarization factor which implies neutrons can only couple to magnetic moments or spin fluctuations perpendicular to ***Q***; *ħω* = energy change experienced by the sample; *ω* = angular frequency of neutron.

In the scattering processes, some neutrons transfer energies with the sample during the scattering process, thus changing both their direction and energy in what is thus inelastic neutron scattering (INS). There are two types of INS instruments, *direct-geometry* and *indirect-geometry* time-of-flight (TOF) spectrometers. Their features and use for coordination chemistry research have been reviewed [77]. In a direct-geometry spectrometer, the selected incident energy E_i is fixed (monochromatic) and final energy E_f is measured by TOF to determine the energy transfer (E_i - E_f) [72, 77]. CNCS used in the current work is a direct-geometry instrument [73, 77, 89-91].

The variable-temperature INS spectra of Mn(TPP)Br·$CDCl_3$ (**2·$CDCl_3$**) in Fig. 10-Left confirm that its D value is negative, as for Mn(TPP)Cl (**1**) [28]. The easy-axis ZFS ($D < 0$) was identified for **2·$CDCl_3$** based on temperature dependence of the neutron energy loss (right) side of the spectra. The peaks centered around +3.3 cm^{-1} (= ~3D) are present at low temperatures while the peaks at about +0.8 to +1.4 cm^{-1} (= ~D) become stronger as the temperature is increased to 25 K. This is expected for an easy-axis ($D < 0$) system, as shown in Scheme 2-Right. The multiple peaks around +3.3 cm^{-1} are consistent with the presence of rhombic parameter E for **2·$CDCl_3$**. From the INS data, if $E = 0$, $D = -1.07$ cm^{-1}. This is close to the parameters from HFEPR: $D = -1.091(3)$ cm^{-1} and $|E| = 0.087(2)$ cm^{-1} discussed above.

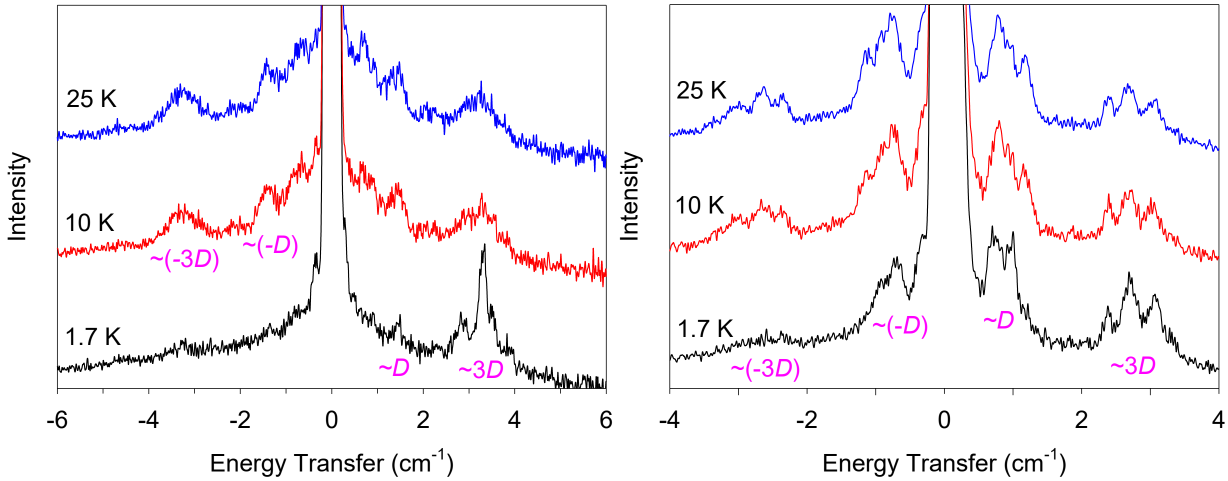

Fig. 10. INS spectra of Mn(TPP)Br·$CDCl_3$ (**2·$CDCl_3$**, Left) and Mn(TPP)I·$CDCl_3$ (**3·$CDCl_3$**, Right) at 1.7, 10 and 25 K. The *E* parameter leads to the splitting of the INS peaks.

Variable-temperature INS spectra of Mn(TPP)I (**3**) in **3·$CDCl_3$** (Fig. 10-Right) point to an easy-plane ($D > 0$) compound based on the neutron energy gain (left) side of the spectra. The peaks around –0.8 to –1.1 cm^{-1} [= ~(-*D*)] are present at low temperatures while the peaks around –2.4 to –3.3 cm^{-1} [= ~(-3*D*)] become stronger as the temperature is increased to 25 K. This is expected for an easy-plane ($D > 0$) system (Scheme 2-Left). At lower temperatures of 1.7 and 10 K, most molecules are at the $M_S = 0$ and ±1 states. Relaxation from the $M_S = \pm1$ states to $M_S = 0$ state gives the peaks around –0.8 to –1.1 cm^{-1}. When the temperature is at 25 K, more molecules are at the $M_S = \pm2$ states which relax back to the $M_S = \pm1$ states, making the higher energy peaks around –2.4 to –3.3 cm^{-1} stronger. The multiple INS peaks, such as those around ~*D* and ~3*D*, are consistent with the presence of rhombic parameter *E* for **3·$CDCl_3$**. If $E = 0$, the INS spectra gave $D \approx 0.90$ cm^{-1}. Although the value is close $D = 1.30$ cm^{-1} and $E = 0.01$ cm^{-1} by HFEPR discussed above, the result also demonstrates that *E*, although small, is critical here.

It is interesting to point out the trend in *D* values for Mn(TPP)Cl (**1**), Mn(TPP)Br (**2**) and

Mn(TPP)I (**3**): −2.24, −1.09, and +1.30 cm^{-1}, respectively [28]. The degree of axial anisotropy decreases from the chloride to the bromide analog. Such decreases of axial anisotropy from chloride to bromide analogs have been reported in other Mn(III) chlorides and bromides such as $Mn(Me_2dbm)X$ (X = Cl, Br; Me_2dbm^- = anion of 4,4'-dimethyldibenzoylmethane) and Mn(OEP)X (X = Cl, Br; OEP^{2-} = 2,3,7,8,12,13,17,18-octaethylporphinate) [92]. A qualitative summary of the studies is given here. For the Mn(III) chloride and bromide complexes such as Mn(OEP)X, the second-order spin-orbital couplings of the four unpaired electrons in the ground electronic quintet state are with the excited electronic states from d-d transitions in the Mn(III) ion [59, 92, 93]. Such ZFS generates easy-axis ($D < 0$) ZFS states, as the equatorial ligand field between the Mn(III) ion and the four N atoms of the OEP^{2-} ligand dominates the spin-orbital couplings. Since both Cl^- and Br^- complexes have the same equatorial ligand OEP^{2-}, the axial ligand field (along the Mn−X axis) determines the magnitude of the $|D|$. This decrease in $|D|$ is primarily due to a weaker axial ligand field for the Br^- complex than its Cl^- analog [92]. We think the decrease in $|D|$ from Mn(TPP)Cl (**1**) to Mn(TPP)Br (**2**) is similar to those in $Mn(Me_2dbm)X$ and Mn(OEP)X.

How to understand that the iodide analog Mn(TPP)I (**3**) becomes an easy-plane ($D > 0$) complex? Such an change from easy-axis ($D < 0$) to easy-plane ($D > 0$) between metal halide analogs has been reported in Mn(III) complexes *trans*-$[Mn(cyclam)Br_2]Br$ (cyclam = 1,4,8,11-tetraazacyclotetradecane) and *trans*-$[Mn(cyclam)I_2]I$ [94]. The positive D value for the iodide analog here is attributed to the presence of ligand-to-metal charge transfer (LMCT) from the lone pair electrons on I^- ions (in *trans*-$[Mn(cyclam)I_2]^-$) to a 3d orbital of the Mn(III) ion, generating low-lying excited electronic LMCT states with atomic iodine character. The second-order spin-orbital interactions of the four unpaired electrons in the ground electronic quintet state of *trans*-

$[Mn(cyclam)I_2]^-$ are primarily mediated by spin-orbit coupling, which is very large for iodine, with the excited electronic LMCT states, leading to the unique easy-plane ($D > 0$) zero-field splitting (ZFS) states [94]. In other words, ZFS in Mn(TPP)Cl (**1**) and Mn(TPP)Br (**2**) are mainly the results of ligand fields on the metal ions, while ZFS in Mn(TPP)I (**3**) reflects the participation of LMCT.

4. Conclusion

The current work shows that manganese tetraphenylporphyrin bromide and iodide Mn(TPP)X (X = Br, **2**; I, **3**) may accommodate different solvents in the lattice. The Mn(III)–Br and Mn(III)–I bonds in $S = 2$ Mn(TPP)X are unexpectedly longer than Fe(III)–Br and Fe(III)–I bonds in $S = 5/2$ Fe(TPP)X (X = Br, **4**; I, **5**). HFEPR and INS studies show that the axial ZFS parameter (D) decreases from Mn(TPP)Cl (**1**) to Mn(TPP)Br (**2**), likely as a result of a weaker axial (Mn–Br) ligand field in **2** than that (Mn–Cl) in **1**. Unlike **1** and **2**, Mn(TPP)I (**3**) has easy-plane anisotropy, presumably as a results of [I^- to Mn(III)] LMCT.

Author contributions

A.N.B. grew crystals of **2·$CHCl_3$**, **2·CH_2Cl_2** and **3·$CHCl_3$**, conducted X-ray single-crystal diffraction studies of **2·$CHCl_3$**, **2·CH_2Cl_2**, **3·$CHCl_3$** and **3·1.5$CHCl_3$** and CShM and Hirshfeld surface calculations with X.W. She performed DC and AC susceptibility measurements using magnetometers with Z.G., Q.C. and H.D.Z. and measurements by the NMR Evans method with C.A.S. S.E.S. prepared the samples of **2** and **3** and grew the crystals of **2·$CDCl_3$** and **3·$CDCl_3$**, conducted INS studies with A.A.P., and studied X-ray single-crystal diffraction of **3·$CDCl_3$**. J.K. and J.T. conducted HFEPR work. Z.L. prepared samples of **2** and **3** and grew crystals of **$3 \cdot 1.5CHCl_3$**. X.B.P. and X.W. resolved crystallographic disorders. X.-T.C. worked with A.N.B. and Z.-L.X. to interpret the magnetic susceptibility results. Z.L., Q.C., C.A.S. and H.D.Z. studied Mn(TPP)F. Z.-L.X. designed and supervised the research. Z.L.X., A.N.B., S.E.S. and J.K. wrote the manuscript with input from all authors.

Declaration of interests

None.

Appendix A. Supplementary data

CCDC 1977353-1977357 contains the supplementary crystallographic data for Mn(TPP)I·$CDCl_3$ (**$3 \cdot CDCl_3$**), Mn(TPP)I·$1.5CHCl_3$ (**$3 \cdot 1.5CHCl_3$**), Mn(TPP)I·$CHCl_3$ (**$3 \cdot CHCl_3$**), Mn(TPP)Br·$CHCl_3$ (**$2 \cdot CHCl_3$**) and Mn(TPP)Br·CH_2Cl_2 (**$2 \cdot CH_2Cl_2$**). These data can be obtained free of charge via http://www.ccdc.cam.ac.uk/conts/retrieving.html, or from the Cambridge Crystallographic Data Centre, 12 Union Road, Cambridge CB2 1EZ, UK; fax: (+44) 1223-336-033; or e-mail: deposit@ccdc.cam.ac.uk.

Acknowledgment

The authors thank financial support by the U.S. National Science Foundation (CHE-1633870 and CHE-1900296 to Z-L.X.; DMR-1350002 to H.D.Z.) and a Shull Wollan Center Graduate Research Fellowship (S.E.S. and Z.L.). Acknowledgment is also made to the Donors of the American Chemical Society Petroleum Research Fund for partial support of this work. Part of this work was done at the National High Magnetic Field Laboratory, which is supported by U.S. National Science Foundation through Cooperative Agreement DMR-1644779 and the State of Florida. Part of the research used resources at the Spallation Neutron Source, a Department of Energy (DOE) Office of Science User Facility operated by ORNL. The magnetic measurements were conducted in part at the Center for Nanophase Materials Sciences, which is a DOE Office of Science User Facility. We thank Dr. A. Ozarowski for the EPR simulation and fitting software SPIN.

References

[1] D. Dolphin, The Porphyrins (7 volumes), Academic Press, New York, 1978-1979.

[2] K.M. Kadish, K.M. Smith, R. Guilard, The Porphyrin Handbook (20 volumes), Academic Press, San Diego, 2000-2003.

[3] K.M. Kadish, K.M. Smith, R. Guilard, Handbook of Porphyrin Science with Applications to Chemistry, Physics, Materials Science, Engineering, Biology and Medicine (5 volumes), World Scientific, Singapore., 2010.

[4] J. Zaleski, Über die Verbindungen des Mesoporphyrins mit Eisen und Mangan, Z. Physiol. Chem., 43 (1905) 11-17.

[5] H. Fischer, J. Hilger, Zur Kenntnis der natürlichen Porphyrine. XVII. Mitteilung. Neue Überführung von Uro- in Koproporphyrin und über einige Derivate dieser Porphyrine, Z. Physiol. Chem., 149 (1925) 65-70.

[6] E.B. Fleischer, J.M. Palmer, T.S. Srivastava, A. Chatterjee, Thermodyamic and kinetic properties of an iron-porphyrin system, J. Am. Chem. Soc., 93 (1971) 3162-3167.

[7] H. Kobayashi, Y. Yanagawa, Electronic Spectra and Electronic Structure of Iron(II) Tetraphenylporphins, Bull. Chem. Soc. Jpn., 45 (1972) 450-456.

[8] L.J. Boucher, Manganese porphyrin complexes. V. Axial interactions in manganese(3) porphyrins, Ann. NY Acad. Sci., 206 (1973) 409-419.

[9] B. Gonzalez, J. Kouba, S. Yee, C.A. Reed, J.F. Kirner, W.R. Scheidt, Manganese(II) porphyrins. Synthesis, structures, and preference for five-coordination, J. Am. Chem. Soc., 97 (1975) 3247-3249.

[10] C.J. Weschler, B.M. Hoffman, F. Basolo, Synthetic oxygen carrier. Dioxygen adduct of a manganese porphyrin, J. Am. Chem. Soc., 97 (1975) 5278-5280.

[11] P. Turner, M.J. Gunter, B.W. Skelton, A.H. White, Crystal Structures of the Pentacoordinate Bromo, Isocyanato, Iodo, Acetato and Isothiocyanato Complexes of the meso-Tetraphenylporphyrinatomanganese Cation, Aust. J. Chem., 51 (1998) 835-852.

[12] P. Turner, M.J. Gunter, B.W. Skelton, A.H. White, The Influence of the Axial Ligand on the Solid-State Structures of Pentacoordinate Manganese Tetraphenylporphyrin Complexes, Aust. J. Chem., 51 (1998) 853-864.

[13] J.K.M. Sanders, N. Bampos, Z. Clyde-Watson, S.L. Darling, J.C. Hawley, H.-J. Kim, C.C. Mak, S.J. Webb, Axial Coordination Chemistry of Metalloporphyrins, in: K.M. Kadish, K.M. Smith, R. Guilard (Eds.) The Porphyrin Handbook, Ref. 2, Academic Press, San Diego, 2000, Vol. 3, pp. 1-48.

[14] G.N. La Mar, F.A. Walker, Proton nuclear magnetic resonance line widths and spin relaxation in paramagnetic metalloporphyrins of chromium(III), manganese(III), and iron(III), J. Am. Chem. Soc., 95 (1973) 6950-6956.

[15] M.F. Powell, E.F. Pai, T.C. Bruice, Study of (tetraphenylporphinato)manganese(III)-catalyzed epoxidation and demethylation using p-cyano-N,N-dimethylaniline N-oxide as oxygen donor in a homogeneous system. Kinetics, radiochemical ligation studies, and

reaction mechanism for a model of cytochrome P-450, J. Am. Chem. Soc., 106 (1984) 3277-3285.

[16] H.J. Callot, R. Ocampo, Geochemistry of Porphyrins, in: K.M. Kadish, K.M. Smith, R. Guilard (Eds.) The Porphyrin Handbook; Ref. 2, Academic Press, San Diego, 2000, Vol. 1, pp. 349-398.

[17] R.H. Filby, G.J. Van Berkel, Geochemistry of Metal Complexes in Petroleum, Source Rocks, and Coals; An Overview, Metal Complexes in Fossil Fuels. Geochemistry, Characterization, and Processing, ACS Symp. Series, 344 (1987) 2-39.

[18] J.W. Buchler, Synthesis and Properties of Metalloporphyrins, in: D. Dolphin (Ed.) The Porphyrins, Ref. 1, Vol. 1, Ch. 10, Academic Press, New Yor, 1978, Vol. 1, pp. 389-483.

[19] J.S. Lindsey, Synthesis of meso-Substituted Porphyrins, in: K.M. Kadish, K.M. Smith, R. Guilard (Eds.) The Porphyrin Handbook, Ref. 2, Academic Press, San Diego, 2000, Vol. 1, pp. 45–118.

[20] P. Rothemund, A New Porphyrin Synthesis. The Synthesis of Porphin, J. Am. Chem. Soc., 58 (1936) 625-627.

[21] G.N. La Mar, F.A. Walker, Proton nuclear magnetic resonance studies of high-spin manganese(III) complexes with synthetic porphyrins, J. Am. Chem. Soc., 97 (1975) 5103-5107.

[22] R.R. Gaughan, D.F. Shriver, L.J. Boucher, Resonance Raman spectra of manganese(III) tetraphenylporphin halides, Proc. Natl. Acad. Sci. USA, 72 (1975) 433-436.

[23] D.V. Behere, S. Mitra, Magnetic susceptibility study and ground-state zero-field splitting in manganese(III) porphyrins, Inorg. Chem., 19 (1980) 992-995.

[24] H.M. Goff, A.P. Hansen, Carbon-13 and deuterium NMR spectroscopy of high-spin manganese(III) porphyrin halide and pyridine complexes, Inorg. Chem., 23 (1984) 321-326.

[25] D.P. Goldberg, J. Telser, J. Krzystek, A.G. Montalban, L.-C. Brunel, A.G.M. Barrett, B.M. Hoffman, EPR Spectra from "EPR-Silent" Species: High-Field EPR Spectroscopy of Manganese(III) Porphyrins, J. Am. Chem. Soc., 119 (1997) 8722-8723.

[26] J. Mao, Y. Zhang, E. Oldfield, Nuclear Magnetic Resonance Shifts in Paramagnetic Metalloporphyrins and Metalloproteins, J. Am. Chem. Soc., 124 (2002) 13911-13920.

[27] R.-J. Cheng, S.-H. Chang, K.-C. Hung, An Anomalous Spin-Polarization Mechanism in High-Spin Manganese(III) Porphyrin Complexes, Inorg. Chem., 46 (2007) 1948-1950.

[28] S.C. Hunter, A.A. Podlesnyak, Z.-L. Xue, Magnetic Excitations in Metalloporphyrins by Inelastic Neutron Scattering: Determination of Zero-Field Splittings in Iron, Manganese, and Chromium Complexes, Inorg. Chem., 53 (2014) 1955-1961.

[29] A. Pascual-Álvarez, J. Vallejo, E. Pardo, M. Julve, F. Lloret, J. Krzystek, D. Armentano, W. Wernsdorfer, J. Cano, Field-Induced Slow Magnetic Relaxation in a Mononuclear Manganese(III)–Porphyrin Complex, Chem. Eur. J., 21 (2015) 17299-17307.

[30] W.R. Browett, A.F. Fucaloro, T.V. Morgan, P.J. Stephens, Magnetic circular dichroism determination of zero-field splitting in chloro(meso-tetraphenylporphinato)iron(III), J. Am. Chem. Soc., 105 (1983) 1868-1872.

[31] F.A. Walker, Models of the Bis-Histidine-Ligated Electron-Transferring Cytochromes. Comparative Geometric and Electronic Structure of Low-Spin Ferro- and Ferrihemes, Chem. Rev., 104 (2004) 589-616.

[32] F.A. Walker, Magnetic spectroscopic (EPR, ESEEM, Mössbauer, MCD and NMR) studies of low-spin ferriheme centers and their corresponding heme proteins, Coord. Chem. Rev., 185-186 (1999) 471-534.

[33] K.M. Smith, Porphyrins, in: J.A. McCleverty, T.J. Meyer (Eds.) Comprehensive Coordination Chemistry II, Vol. 1, Ch. 1.23, Elsevier, 2004, Vol. 1, pp. 493-506.

[34] S.C. Hunter, B.A. Smith, C.M. Hoffmann, X. Wang, Y.-S. Chen, G.J. McIntyre, Z.-L. Xue, Intermolecular Interactions in Solid-State Metalloporphyrins and Their Impacts on Crystal and Molecular Structures, Inorg. Chem., 53 (2014) 11552-11562.

[35] S.E. Stavretis, M. Atanasov, A.A. Podlesnyak, S.C. Hunter, F. Neese, Z.-L. Xue, Magnetic Transitions in Iron Porphyrin Halides by Inelastic Neutron Scattering and Ab Initio Studies of Zero-Field Splittings, Inorg. Chem., 54 (2015) 9790-9801.

[36] T. Ohya, M. Sato, Comparative study of Mössbauer spectra of iron(III) complexes of para-substituted tetraphenylporphyrins. Electronic effects of substituents and axial ligands, Dalton Trans., (1996) 1519-1523.

[37] R. Boča, Zero-field splitting in metal complexes, Coord. Chem. Rev., 248 (2004) 757-815.

[38] J. Telser, EPR Interactions – Zero-Field Splittings, in: eMagRes, 2017, Vol. 6, pp. 207-234.

[39] D.G. McGavin, Symmetry constraints on EPR spin-Hamiltonian parameters, J. Magn. Reson., 74 (1987) 19-55.

[40] B. Cheng, W.R. Scheidt, Chloro(5,10,15,20-tetraphenylporphyrinato)manganese(III) with 4/m Symmetry, Acta Cryst. C, 52 (1996) 361-363.

[41] C. Cohen-Tannoudji, B. Diu, F. Laloe, Quantum Mechanics, Wiley, 1977, pp. 1078, 1313.

[42] K.A. Campbell, M.R. Lashley, J.K. Wyatt, M.H. Nantz, R.D. Britt, Dual-Mode EPR Study of Mn(III) Salen and the Mn(III) Salen-Catalyzed Epoxidation of cis-β-Methylstyrene, J. Am. Chem. Soc., 123 (2001) 5710-5719.

[43] J. Krzystek, J. Telser, High frequency and field EPR spectroscopy of Mn(III) complexes in frozen solutions, J. Magn. Reson., 162 (2003) 454-465.

[44] J. Krzystek, G.J. Yeagle, J.-H. Park, R.D. Britt, M.W. Meisel, L.-C. Brunel, J. Telser, High-Frequency and -Field EPR Spectroscopy of Tris(2,4-pentanedionato)manganese(III): Investigation of Solid-State versus Solution Jahn−Teller Effects, Inorg. Chem., 42 (2003) 4610-4618.

[45] R. Gupta, T. Taguchi, A.S. Borovik, M.P. Hendrich, Characterization of Monomeric MnII/III/IV–Hydroxo Complexes from X- and Q-Band Dual Mode Electron Paramagnetic Resonance (EPR) Spectroscopy, Inorg. Chem., 52 (2013) 12568-12575.

[46] J. Krzystek, A. Schnegg, A. Aliabadi, K. Holldack, S.A. Stoian, A. Ozarowski, S.D. Hicks, M.M. Abu-Omar, K.E. Thomas, A. Ghosh, K.P. Caulfield, Z.J. Tonzetich, J. Telser, Advanced Paramagnetic Resonance Studies on Manganese and Iron Corroles with a Formal d4 Electron Count, Inorg. Chem., 59 (2020) 1075-1090.

[47] K.A. Campbell, E. Yikilmaz, C.V. Grant, W. Gregor, A.-F. Miller, R.D. Britt, Parallel Polarization EPR Characterization of the Mn(III) Center of Oxidized Manganese Superoxide Dismutase, J. Am. Chem. Soc., 121 (1999) 4714-4715.

[48] R.D. Britt, J.M.P. and, K.A. Campbell, Pulsed and Parallel-Polarization EPR Characterization of the Photosystem II Oxygen-Evolving Complex, Annu. Rev. Biophys. Biomol. Struct., 29 (2000) 463-495.

[49] M.P. Hendrich, P.G. Debrunner, Integer-spin electron paramagnetic resonance of iron proteins, Biophys. J., 56 (1989) 489-506.

[50] J.J. McKinnon, D. Jayatilaka, M.A. Spackman, Towards quantitative analysis of intermolecular interactions with Hirshfeld surfaces, Chem. Commun., (2007) 3814-3816.

[51] M.A. Spackman, D. Jayatilaka, Hirshfeld surface analysis, CrystEngComm, 11 (2009) 19-32.

[52] M.A. Spackman, J.J. McKinnon, Fingerprinting intermolecular interactions in molecular crystals, CrystEngComm, 4 (2002) 378-392.

[53] J.J. McKinnon, M.A. Spackman, A.S. Mitchell, Novel tools for visualizing and exploring intermolecular interactions in molecular crystals, Acta Cryst. B, 60 (2004) 627-668.

[54] M.J. Turner, J.J. McKinnon, D. Jayatilaka, M.A. Spackman, Visualisation and characterisation of voids in crystalline materials, CrystEngComm, 13 (2011) 1804-1813.

[55] L.J. Boucher, J.W. Klinehamer, Manganese porphyrin complexes. VII. chloro(α,β,γ,δ, tetraphenylchlorin) manganese (III), Bioinorg. Chem., 2 (1973) 231-241.

[56] Y. Nakato, K. Abe, H. Tsubomura, Experimental determination of ionization potentials of tetraphenylporphine and metallotetraphenylporphines, Chem. Phys. Lett., 39 (1976) 358-360.

[57] R.S. Armstrong, G.J. Foran, T.W. Hambley, Structure of chloro(α,β,γ,δ-tetra-phenylporphinato)manganese(III) toluene solvate, Acta Cryst. C, 49 (1993) 236-238.

[58] F. Paulat, V.K.K. Praneeth, C. Näther, N. Lehnert, Quantum Chemistry-Based Analysis of the Vibrational Spectra of Five-Coordinate Metalloporphyrins [M(TPP)Cl], Inorganic Chemistry, 45 (2006) 2835-2856.

[59] J. Krzystek, J. Telser, L.A. Pardi, D.P. Goldberg, B.M. Hoffman, L.-C. Brunel, High-Frequency and -Field Electron Paramagnetic Resonance of High-Spin Manganese(III) in Porphyrinic Complexes, Inorg. Chem., 38 (1999) 6121-6129.

[60] J. Krzystek, L.A. Pardi, L.-C. Brunel, D.P. Goldberg, B.M. Hoffman, S. Licoccia, J. Telser, High-frequency and -field electron paramagnetic resonance of high-spin manganese(III) in tetrapyrrole complexes, Spectrochim. Acta A, 58 (2002) 1113-1127.

[61] R. Golnak, J. Xiao, M. Pohl, C. Schwanke, A. Neubauer, K.M. Lange, K. Atak, E.F. Aziz, Influence of the Outer Ligands on Metal-to-Ligand Charge Transfer in Solvated Manganese Porphyrins, Inorg. Chem., 55 (2016) 22-28.

[62] C. Duboc, D. Ganyushin, K. Sivalingam, M.-N. Collomb, F. Neese, Systematic Theoretical Study of the Zero-Field Splitting in Coordination Complexes of Mn(III). Density Functional Theory versus Multireference Wave Function Approaches, J. Phys. Chem. A, 114 (2010) 10750-10758.

[63] D.V. Behere, V.R. Marathe, S. Mitra, Low-temperature magnetisation study on manganese(III) porphyrins, Chem. Phys. Lett., 81 (1981) 57-61.

[64] M.G.I. Galinato, E.P. Brocious, F. Paulat, S. Martin, J. Skodack, J.B. Harland, N. Lehnert, Elucidating the Electronic Structure of High-Spin [$\mathrm{Mn^{III}}$(TPP)Cl] Using Magnetic Circular Dichroism Spectroscopy, Inorg. Chem., 59 (2020) 2144-2162.

[65] A. Tulinsky, B.M.L. Chen, The crystal and molecular structure of chloro-α,β,γ,δ-tetraphenylporphinatomanganese(III), J. Am. Chem. Soc., 99 (1977) 3647-3651.

[66] B.J. Kennedy, K.S. Murray, Magnetic properties and zero-field splitting in high-spin manganese(III) complexes. 2. Axially ligated manganese(III) porphyrin complexes, Inorg. Chem., 24 (1985) 1557-1560.

[67] D.H. Moseley, S.E. Stavretis, K. Thirunavukkuarasu, M. Ozerov, Y. Cheng, L.L. Daemen, J. Ludwig, Z. Lu, D. Smirnov, C.M. Brown, A. Pandey, A.J. Ramirez-Cuesta, A.C. Lamb, M. Atanasov, E. Bill, F. Neese, Z.-L. Xue, Spin–phonon couplings in transition metal complexes with slow magnetic relaxation, Nat. Commun., 9 (2018) 2572.

[68] S.E. Stavretis, Y. Cheng, L.L. Daemen, C.M. Brown, D.H. Moseley, E. Bill, M. Atanasov, A.J. Ramirez-Cuesta, F. Neese, Z.-L. Xue, Probing Magnetic Excitations in Co^{II} Single-Molecule Magnets by Inelastic Neutron Scattering, Eur. J. Inorg. Chem., 2019 (2019) 1119-1127.

[69] S.E. Stavretis, E. Mamontov, D.H. Moseley, Y. Cheng, L.L. Daemen, A.J. Ramirez-Cuesta, Z.-L. Xue, Effect of magnetic fields on the methyl rotation in a paramagnetic cobalt(ii) complex. Quasielastic neutron scattering studies, Phys. Chem. Chem. Phys., 20 (2018) 21119-21126.

[70] L. Chen, H.-H. Cui, S.E. Stavretis, S.C. Hunter, Y.-Q. Zhang, X.-T. Chen, Y.-C. Sun, Z. Wang, Y. Song, A.A. Podlesnyak, Z.-W. Ouyang, Z.-L. Xue, Slow magnetic relaxations in cobalt(II) tetranitrate complexes. Studies of magnetic anisotropy by inelastic neutron scattering and high-frequency and high-field EPR spectroscopy, Inorg. Chem., 55 (2016) 12603-12617.

[71] S.E. Stavretis, D.H. Moseley, F. Fei, H.-H. Cui, Y. Cheng, A.A. Podlesnyak, X. Wang, L.L. Daemen, C.M. Hoffmann, M. Ozerov, Z. Lu, K. Thirunavukkuarasu, D. Smirnov, T. Chang, Y.-S. Chen, A.J. Ramirez-Cuesta, X.-T. Chen, Z.-L. Xue, Spectroscopic Studies of the Magnetic Excitation and Spin-Phonon Couplings in a Single-Molecule Magnet, Chem. Eur. J., 25 (2019) 15846-15857.

[72] A. Furrer, J. Mesot, T. Strässle, Neutron Scattering in Condensed Matter Physics, World Scientific Publishing Company, 2009, pp. 12-13, 17.

[73] J.M. Carpenter, C.K. Loong, Elements of Slow-Neutron Scattering: Basics, Techniques, and Applications, Cambridge University Press, Cambridge, 2015.

[74] K.S. Pedersen, M.A. Sørensen, J. Bendix, Fluoride-coordination chemistry in molecular and low-dimensional magnetism, Coord. Chem. Rev., 299 (2015) 1-21.

[75] M.J. Turner, J.J. McKinnon, S.K. Wolff, D.J. Grimwood, P.R. Spackman, D. Jayatilaka, M.A. Spackman, in, University of Western Australia. http://hirshfeldsurface.net, 2017.

[76] A.K. Hassan, L.A. Pardi, J. Krzystek, A. Sienkiewicz, P. Goy, M. Rohrer, L.C. Brunel, Ultrawide Band Multifrequency High-Field EMR Technique: A Methodology for Increasing Spectroscopic Information, J. Magn. Reson., 142 (2000) 300-312.

[77] Z.-L. Xue, A.J. Ramirez-Cuesta, C.M. Brown, S. Calder, H. Cao, B.C. Chakoumakos, L.L. Daemen, A. Huq, A.I. Kolesnikov, E. Mamontov, A.A. Podlesnyak, X. Wang, Neutron Instruments for Research in Coordination Chemistry, Eur. J. Inorg. Chem., 2019 (2019) 1065-1089.

[78] R. Basler, C. Boskovic, G. Chaboussant, H.U. Güdel, M. Murrie, S.T. Ochsenbein, A. Sieber, Molecular Spin Clusters: New Synthetic Approaches and Neutron Scattering Studies, ChemPhysChem, 4 (2003) 910-926.

[79] R.T. Azuah, L.R. Kneller, Y. Qiu, P.L.W. Tregenna-Piggott, C.M. Brown, J.R.D. Copley, R.M. Dimeo, DAVE: A Comprehensive Software Suite for the Reduction, Visualization, and Analysis of Low Energy Neutron Spectroscopic Data, J. Res. Natl. Inst. Stand. Technol., 114 (2009) 341-358.

[80] S. Alvarez, P. Alemany, D. Casanova, J. Cirera, M. Llunell, D. Avnir, Shape maps and polyhedral interconversion paths in transition metal chemistry, Coord. Chem. Rev., 249 (2005) 1693-1708.

[81] J. Cirera, E. Ruiz, S. Alvarez, Continuous Shape Measures as a Stereochemical Tool in Organometallic Chemistry, Organometallics, 24 (2005) 1556-1562.

[82] R.D. Shannon, Revised effective ionic radii and systematic studies of interatomic distances in halides and chalcogenides, Acta Cryst. A, 32 (1976) 751-767.

[83] B. Skelton, A. White, Crystal structure of Bromo(tetraphenylporphyrin)iron(III), Aus. J. Chem., 30 (1977) 2655-2660.

[84] K. Hatano, W.R. Scheidt, Molecular stereochemistry of iodo(meso-tetraphenylporphinato)iron(III), Inorg. Chem., 18 (1979) 877-879.

[85] E. Collet, P. Guionneau, Structural analysis of spin-crossover materials: From molecules to materials, C. R. Chimie, 21 (2018) 1133-1151.

[86] W.R. Scheidt, Systematics of the Stereochemistry of Porphyrins and Metalloporphyrins, in: K.M. Kadish, K.M. Smith, R. Guilard (Eds.) The Porphytin handbook, Academic Press, 2000, Vol. 3, pp. 49-112.

[87] J. Krzystek, S.A. Zvyagin, A. Ozarowski, S. Trofimenko, J. Telser, Tunable-frequency high-field electron paramagnetic resonance, J. Magn. Reson., 178 (2006) 174-183.

[88] G.E. Bacon, Neutron Scattering in Chemistry, Butterworth, London, 1977.

[89] G. Ehlers, A.A. Podlesnyak, J.L. Niedziela, E.B. Iverson, P.E. Sokol, The new cold neutron chopper spectrometer at the Spallation Neutron Source: Design and performance, Rev. Sci. Instrum., 82 (2011) 085108.

[90] CNCS website: https://neutrons.ornl.gov/cncs

[91] P.C.H. Mitchell, S.F. Parker, A.J. Ramirez-Cuesta, J. Tomkinson, Vibrational Spectroscopy with Neutrons: With Applications in Chemistry, Biology, Materials Science and Catalysis, World Scientific Publishing Company, 2005, pp. 552-558.

[92] J. Krzystek, J. Telser, M.J. Knapp, D.N. Hendrickson, G. Aromí, G. Christou, A. Angerhofer, L.C. Brunel, High-frequency and -field electron paramagnetic resonance of high-spin manganese(III) in axially symmetric coordination complexes, Appl. Magn. Reson., 21 (2001) 571-585.

[93] L.B. Dugad, D.V. Behere, V.R. Marathe, S. Mitra, Magnetic properties and electronic structure of manganese(III) porphyrins, Chem. Phys. Lett., 104 (1984) 353-356.

[94] S. Mossin, H. Weihe, A.-L. Barra, Is the Axial Zero-Field Splitting Parameter of Tetragonally Elongated High-Spin Manganese(III) Complexes Always Negative?, J. Am.Chem. Soc., 124 (2002) 8764-8765.

Graphical abstract

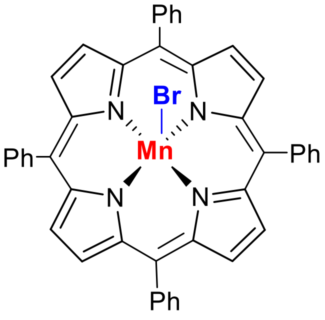

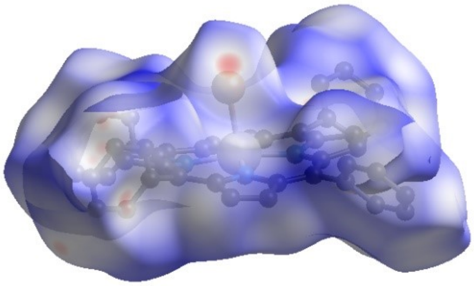

Mn–Br/I bonds in Mn(TPP)X are surprisingly longer than Fe–Br/I bonds in Fe(TPP)X (X = Br, I), although Mn(III) and Fe(III) ions have the same radii. Mn(TPP)Br has easy-axis anisotropy ($D < 0$), while Mn(TPP)I is easy-plane ($D > 0$). Magnitude of the axial anisotropy decreases from Mn(TPP)Cl to Mn(TPP)Br.